CHAPTER TWO

Roadmap of exploring self-assembly and the self-organization of nanoscale polyoxometalate clusters

De-Liang Long* **and Leroy Cronin***
School of Chemistry, The University of Glasgow, Glasgow, G12 8QQ, United Kingdom
*Corresponding authors. e-mail address: deliang.long@glasgow.ac.uk; lee.cronin@glasgow.ac.uk

Contents

Abstract

Polyoxometalates (POMs) have undergone rapid development over the past decade, emerging as one of the most versatile classes of inorganic molecular clusters with broad applications in catalysis, energy conversion, nanotechnology, and biomedicine. This chapter highlights several fast-evolving areas in POM research, with a focus on the self-assembly and self-organisation of novel structures and composites. Particular emphasis is placed on innovative synthetic methodologies, unprecedented structural diversity, and controlled self-assembly processes at the nanoscale. We showcase groundbreaking advances in giant molybdenum blue/red systems, high-nuclearity

Advances in Inorganic Chemistry, Volume 86
ISSN 0898-8838, https://doi.org/10.1016/bs.adioch.2025.09.001

polyoxoniobate clusters, non-classical POMs, atomically precise silver-POM hybrids, and mixed-metal architectures. This chapter provides an in-depth analysis of organic ligand-directed assembly strategies that have enabled the construction of new classes of POM-based cages and metal-organic frameworks. Special attention is given to emerging research directions, including supramolecular assembly, nanoscale POM materials, and bio-inspired POM systems. The structure-property relationships that underpin POM functionality in catalysis, energy storage, and biomedical applications are briefly evaluated. Finally, we present a forward-looking perspective on the challenges and opportunities in the field, including AI-guided molecular design, simulation of reaction mechanisms and assembly process, and the integration of POMs into functional materials. With over 160 references to the most impactful studies of the past decade, this chapter serves as a comprehensive roadmap to future developments in POM self-assembly and self-organization.

1. Introduction

Polyoxometalates (POMs) constitute a distinctive class of anionic metal-oxo clusters that have been a subject of scientific interest since Berzelius' discovery of ammonium phosphomolybdate in 1826.[1] These compounds, primarily formed by early transition metals (e.g., V, Nb, Mo, and W) in their highest oxidation states, display remarkable structural diversity, ranging from simple Lindqvist $\{M_6O_{19}\}$[2] and Keggin $\{XM_{12}O_{40}\}$[3] architectures to highly complex, giant assemblies with nuclearities exceeding 300 metal centers.[4] POMs can be categorized into two main types: isoPOMs, which consist of a single metal species, and heteroPOMs, which incorporate heteroatoms (typically p-block elements) or additional metal substituents. The inclusion of heteroatoms and partial metal substitutions results in exceptional compositional versatility, with POM structures encompassing atomic counts ranging from tens to thousands. This structural and compositional flexibility[5] directly translates into diverse functional applications,[6–8] demonstrated in catalysts,[9–12] electronic devices[13–15] and advanced materials,[16–19] leveraging their unique redox, spectroscopic, photovoltaic, and magnetic properties.

The past decade has witnessed a paradigm shift in POM chemistry, moving beyond traditional structural motifs[20] to embrace (1) precision synthesis of giant clusters with atomic-level control[5,21]; (2) hybrid materials integrating POMs with organic frameworks, nanoparticles, and biomolecules[22–24]; (3) dynamic systems exhibiting stimuli-responsive assembly/disassembly[25]; (4) functional materials with tailored electronic, magnetic, and optical properties.[26–29] This comprehensive chapter is organized into five major sections that reflect the most impactful developments in POM research, focusing on the self-assembly and self-organization, over the past decade. The topics include synthesis methods, new POM structures, POM-organic hybrids, POM-based high order materials and perspective.

2. Synthetic methodologies

2.1 Traditional synthesis approaches

The foundation of POM chemistry remains the acid-base condensation of metal ion precursors in aqueous solution. The classic "one-pot" synthesis of typical POM clusters such as $\{Mo_{154}\}$[30] and $\{P_5W_{30}\}$[31] involves careful pH control and has been optimised over decades. Recent refinements include pH-controlled assembly: (1) systematic studies have established precise pH windows for different POM types, e.g. various lacunary species of polyoxotungstates (W-POMs)[5]; (2) counterion effects,[32] such as the role of aminium as cations in directing structure formation,[33] have been quantified through high-throughput screening; (3) temperature gradients and time resolved assembly enables crystallization of metastable phases.[34]

2.2 Advanced synthetic strategies

Hydrothermal and solvothermal methods are well-established in synthetic chemistry and remain essential for preparing POM-organic hybrid materials. Recent developments demonstrate that high-temperature (100–200 °C) sealed reactions enable novel POM architectures. For example, most large polyoxoniobates (Nb-POMs) are synthesized hydrothermally. While molybdenum blues (MBs) were traditionally prepared at room temperature due to the presumed instability of Mo^V, higher temperatures have now been shown to stabilize unique structures, such as the neutral $\{Mo_{90}Ln_{10}\}$ framework formed at 100 °C.[35] Hydrothermal approach has also enabled the synthesis of giant clusters like $\{Mo_{240}\}$[36] and many other Mo reds,[37] expanding the scope of accessible POM compositions. The challenge of hydrothermal and solvothermal synthesis is the difficulty in monitoring the reaction progress in real-time due to the sealed nature of the system, making it harder to optimize conditions dynamically.

Microwave-assisted synthesis efficiently fabricates POMs and their hybrid materials, offering rapid, uniform heating, higher yields, shorter reaction times, and energy savings. The fast, homogeneous heating enables kinetic control over assembly.[38] For example, nonaqueous microwave conditions yielded novel molybdovanadates.[39] Additionally, POM-capped gold nanoparticles were obtained by heating $AuNO_3(PMe_3)$ in acetonitrile with POM species and tetrabutylammonium at 120 °C.[40] A solid-liquid-gas three-phase electrolysis system using microwave-synthesized POM-based MOFs was developed to convert disulfide substrates into valuable C–S bond-containing products, such as anticancer drugs.[41]

Electrosynthesis offers a clean, efficient, and controllable route for POM assembly. By using electrons as reducing reagents, it eliminates the need for chemical reductants, reducing waste and simplifying purification. Precise control over redox conditions enables selective formation of reduced or mixed-valence POMs, including complex architectures like MBs. This method also facilitates in situ tuning and monitoring of reactions, making it ideal for accessing novel POM structures and integrating them into electroactive materials. By using electrochemical synthesis, Cronin et al.[42] have shown the productions of various giant polyoxomolybdates (Mo-POMs), with unique structure features, improved yield, increased reproducibility, and shorter crystallization time compared to chemical reduction methods. Falaise et al. used the electrosynthesis method to over-reduce "Wells-Dawson-like" $\{AsW_{18}\}$ POM and yielded species containing a W-W bonded $\{W_3^{IV}\}$ triad and novel chiral structure $\{AsW_{26}\}$ (Fig. 1).[43] A parallel work produced metal-metal bonded mixed metal triad $\{Mo^{IV}W_2^{IV}\}$ in Keggin cluster $\{SiMoW_{11}\}$.[44] A facile electrosynthesis method uniformly disperses Wells-Dawson- and Keggin-type POMs on TiO_2 nanotube arrays, resulting in a series of single-cluster functionalized catalysts $\{P_2M_{18}@TiO_2\}$ and $\{PM_{12}@TiO_2\}$ (M = Mo or W).[45] The single POM clusters serves as electronic sponge to accept electrons from excited TiO_2 for enhancing surface-hole concentration and promote water oxidation.

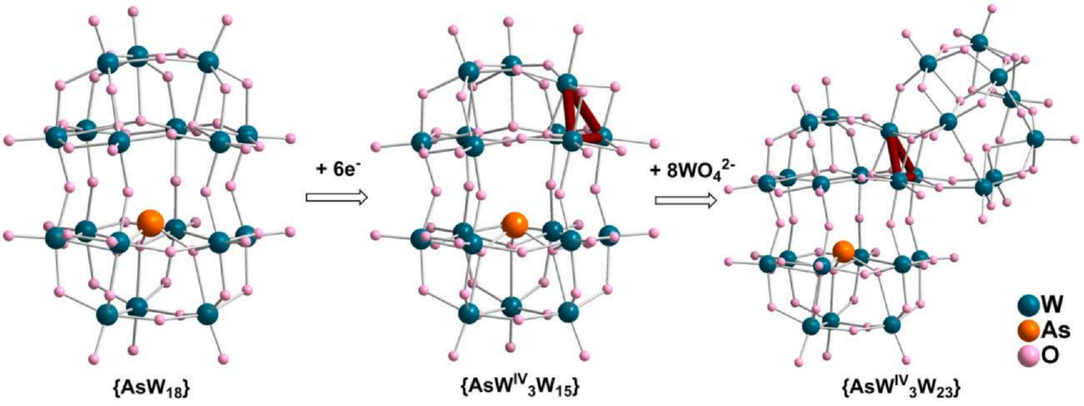

Fig. 1 Electrosynthesis of super-reduced "Wells-Dawson-like" POM $\{AsW_3^{IV}W_{15}\}$ and $\{AsW_3^{IV}W_{23}\}$.

Other cutting-edge approaches include photochemical[46] and mechanochemical synthesis.[47] In a recent study,[47] $\{PMo_{12}\}$ was reacted with n equiv of lithium metal (n = 1–24), yielding a mixture of variably reduced $\{PMo_{12}\}$ species. Analysis revealed Mo-Mo bond formation beginning at n = 8 and a major structural change at n > 12. At n = 24, the results indicated the formation of at least one Mo^{IV}-Mo^{IV} bonded $\{Mo_3^{IV}\}$ triad alongside multiple Mo^{V} centres. This work uncovers complex, unexplored chemistry in super-reduced POMs and introduces a solvent-free method to advance the fundamental understanding of electronic properties and reactivity of electron-rich nanoscale metal oxides.

The synthesis of POM clusters remains a significant challenging due to their reliance on highly sensitive synthetic conditions, which generate a vast array of potential building blocks (BBs) and subunits, making precise control difficult. Achieving well-defined POM structures is crucial for understanding of the fundamental relationship between each building motif's structure and function. However, atomic-level tailoring of specific sites within POMs, while preserving the integrity of their overall framework, remains an exceptional challenge.

3. Building block strategy for growing gigantic POM clusters

3.1 Advances in Mo blues

A particularly fascinating subgroup of POMs comprises the giant nanosized Mo-based clusters, which contain hundreds of Mo atoms and approach protein dimensions.[48] The chemistry of giant Mo-POMs emerged in 1996 when Müller and co-workers determined the crystal structure of the first mixed valent, wheel-shaped $\{Mo_{154}\}$,[30] containing 28 Mo^{V} centres. Subsequent work expanded this family to include the Keplerate K-$\{Mo_{132}\}$,[49] ball-shaped $\{Mo_{102}\}$,[50] wheel-shaped $\{Mo_{176}\}$,[51,52] capped wheel $\{Mo_{248}\}$[53] and lemon-shaped $\{Mo_{368}\}$[4] architectures. Traditionally classified by their coloration as Mo-blue or Mo-brown (represented by K-$\{Mo_{132}\}$), these giant clusters share common structural features. All contain transferable pentagonal $\{Mo_6\}$ or their derived $\{Mo_8\}$ BBs, combined with various supporting/templating and bridging units (Fig. 2). The archetypal $\{Mo_{154}\}$[30] and $\{Mo_{176}\}$ wheels,[51,52] for instance, consist of 14 or 16 $\{Mo_8\}$ units (tetradecamer or hexadecamer), interconnected by backbone-supporting $\{Mo_1\text{-s}\}$ units and corner-sharing $\{Mo_2\text{-c}\}$ bridging "skirt" units along the

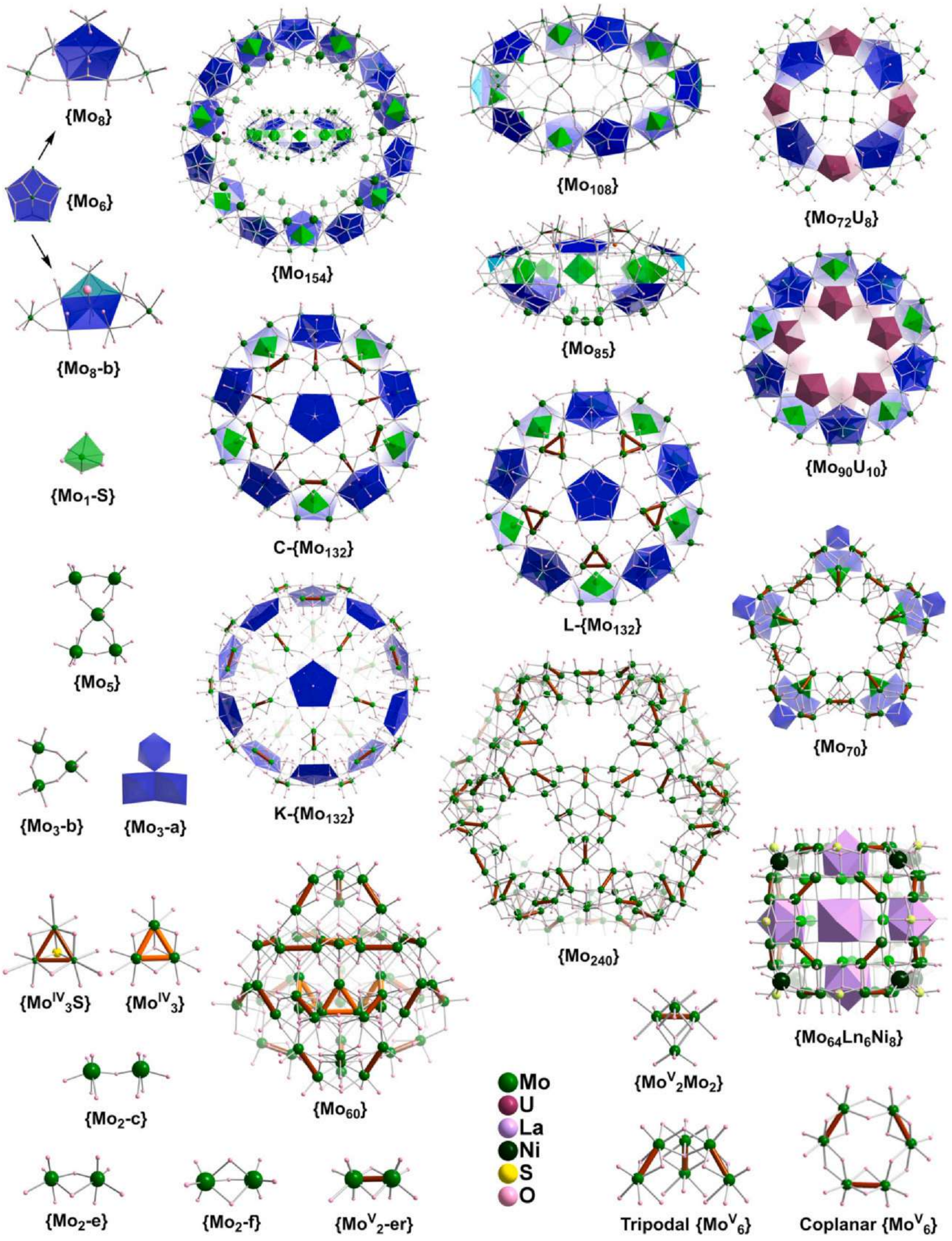

Fig. 2 Main building blocks for Mo-POMs include pentagon $\{Mo_6\}$, normal pentagon based $\{Mo_8\}$ and bent pentagon based $\{Mo_8\text{-b}\}$, supporting $\{Mo_1\text{-s}\}$, bridging $\{Mo_3\text{-b}\}$, add-on $\{Mo_3\text{-a}\}$, corner sharing $\{Mo_2\text{-c}\}$, edge sharing $\{Mo_2\text{-e}\}$, face sharing $\{Mo_2\text{-f}\}$, reduced edge sharing $\{Mo^V_2\text{-er}\}$. Representative Mo blue and Mo red structures from $\{Mo_{154}\}$ to $\{Mo_{64}\}$. In$\{Mo_{154}\}$ top view, a side view copy is inside the wheel.

wheel edges (Fig. 2). In contrast, the K-$\{Mo_{132}\}$[49] and ball-shaped $\{Mo_{102}\}$[50] clusters feature distinct architecture, with 12 $\{Mo_6\}$ pentagons connected by 30 $\{Mo_2\text{-er}\}$ (Mo^V-Mo^V bonded, Fig. 2) or $\{Mo_1\text{-b}\}$ bridges. The cluster size and curvature of the wheels are regulated by the $\{Mo_2\text{-c}\}$ linker length, which accounts for the limited accessibility of other ring sizes within this structural family beyond $\{Mo_{154}\}$[30] and $\{Mo_{176}\}$.[51,52] Late studies enabled the synthesis of smaller analogs through partial replacement of $\{Mo_2\text{-c}\}$ units with lanthanide (Ln) bridges, yielding clusters such as $\{Mo_{128}Ln_2\}$,[54] $\{Mo_{124}Ln_4\}$,[55–58] $\{Mo_{120}Ln_6\}$,[59] and $\{Mo_{90}Ln_{10}\}$[35] containing 10–12 $\{Mo_8\}$ BBs (decamer or dodecamer).

Most recent advances have further diversified this family through the incorporation of $\{Mo_3S\}$, edge-sharing $\{Mo_2\text{-er}\}$ and uranyl bridges, leading to novel structures like lantern shaped L-$\{Mo_{132}\}$,[60] capped wheel C-$\{Mo_{132}\}$[61] and wheel shaped $\{Mo_{90}U_{10}\}$[62] (Fig. 2). All three structures share the same decamer backbone construction, although L-$\{Mo_{132}\}$[60] and C-$\{Mo_{132}\}$[61] are further capped by two additional pentagonal $\{Mo_6\}$ units at their two ends. Fascinatingly, L-$\{Mo_{132}\}$ and C-$\{Mo_{132}\}$ share the same nuclearity as K-$\{Mo_{132}\}$,[49] but their framework differ substantially. While K-$\{Mo_{132}\}$ exhibits icosahedral symmetry, L-$\{Mo_{132}\}$ and C-$\{Mo_{132}\}$ adopt rare oblate spheroid geometries with D_{5d} symmetry. The $\{Ce_{11}Mo_{96}\}$ cluster[61] represents an intriguing hybrid, combining structure elements similar to hemispheres of $\{Mo_{90}Ce_{10}\}$ and C-$\{Mo_{132}\}$. Burns et al.[62] reported the first uranium-containing MB clusters, $\{Mo_{72}U_8\}$, $\{Mo_{97}U_{10}\}$ and $\{Mo_{90}U_{10}\}$, along with their unique properties arising from uranium incorporation. $\{Mo_{72}U_8\}$ represents unconventional square-shaped POM, consisting of two face-to-face square shells connected by eight edge-sharing $\{Mo_2\text{-e}\}$ dimers in a spiral-twist configuration, rendering the cluster chiral (Fig. 2). However, it crystallizes as a racemic mixture. Each shell is constructed from four pentagonal $\{Mo_6\}$ units. In principle, the two shells of the chiral $\{Mo_{72}U_8\}$ molecule should be symmetrically equivalent and related by twofold rotation axes. However, structural analysis revealed significant distortion in the solid state, resulting in asymmetrical shells with distinct bonding geometries. This distortion creates an interesting electronic asymmetry, where one shell becomes more negatively charged due to electron localization while the opposite shell remains relatively positive. Remarkably, $\{Mo_{72}U_8\}$ is an octameric MB-type cluster with an unusual 24-electron reduction. The $\{Mo_{97}U_{10}\}$ has a wheel structure similar to $\{Mo_{90}U_{10}\}$ but with an additional heptamolybdate cap on one face.

Latest studies have demonstrated that the geometry of giant Mo-POMs can be controlled through incorporation of alternative supporting/templating groups, including SO_3^{2-} and SO_4^{2-} anions, along with distorted bent pentagonal {Mo_8-b} units. This approach has yielded several architecturally unique clusters including {Mo_{85}} and {Mo_{108}}.[63] The ellipsoidal {Mo_{85}} cluster features a distinctive asymmetric construction with two non-equivalent hemispherical shells. Its octameric belt adopts an elliptical rather than circular geometry, where {Mo_3S} and {Mo_5} bridging units span the wide gaps to complete the cage structure (Fig. 2). In contrast, the decameric {Mo_{108}} cluster forms a closed ellipsoid with centrosymmetric top and bottom sections, each comprising four regular {Mo_8} units and one bent {Mo_8-b} BBs (Fig. 2). A structurally innovative feature of both {Mo_{85}} and {Mo_{108}} is their interlocking assembly mechanism, where the bent apex of each {Mo_8-b} precisely occupies the notch formed between two regular {Mo_8} BBs. These clusters maintain specific {Mo_8-b} to {Mo_8} ratios of 2:6 and 2:8, respectively. While regular {Mo_8} units alone can form classical MB clusters like {Mo_{154}} and {Mo_{176}}, the incorporation of bent {Mo_8-b} BBs requires corporative assembly with regular {Mo_8} BBs to achieve high-nuclearity architectures. It was proposed that these incorporation ratios are not random but follow defined stoichiometric principles.[63] Successful realization of such designed structures necessitates careful selection of supporting and bridging units. New MB structures {Mo_{158}},[64] {Mo_{160}}[65] and {Mo_{172}}[66] (Video 1) from dimerization of octamers similar to {Mo_{85}} were reported recently.

3.2 New emerging of large Mo red clusters

The characteristic blue coloration of MB-type clusters arises from the delocalization of reducing electrons across the entire cluster framework, resulting in low-energy electronic transitions that produce a distinct absorption band at approximately 750 nm in UV–vis spectra. These clusters are structurally defined by their wheel-like backbone architecture. In contrast, the class traditionally termed "Mo-brown" features localized reducing electrons that form clear Mo^V-Mo^V bonds. Given recent discoveries of structurally similar but red-coloured Mo-POMs, we propose reclassifying this group as "Mo-red" clusters. These Mo-red species exhibit a higher-energy absorption band around 450 nm, reflecting the localized electronic transitions in their isolated Mo^V-Mo^V bonds. Recent advances in Mo-red have yielded remarkable structural diversity, including clusters {Mo_{240}},[36] {Mo_{70}},[67] {Mo_{64}},[67] {Mo_{60}}[37] (Fig. 2) and {Mo_{74}}[68] (Video 2). While MB

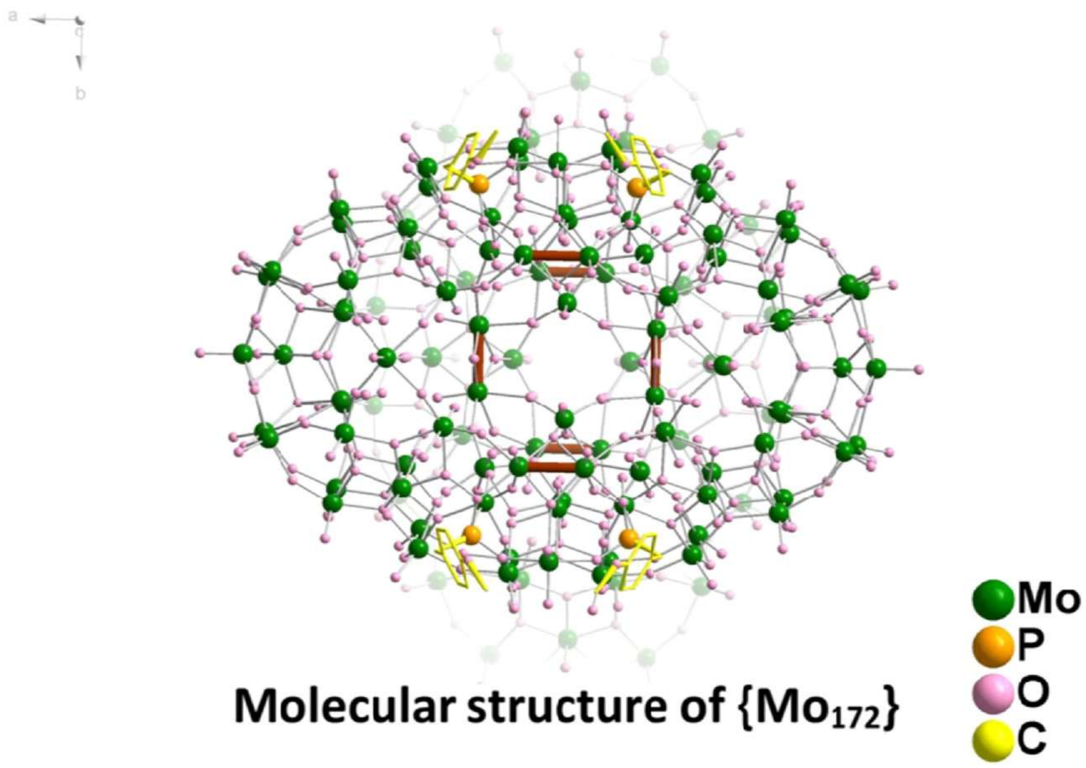

Video 1 A video clip is available online. Supplementary material related to this article can be found online at http://doi.org/10.1016/bs.adioch.2025.09.001.

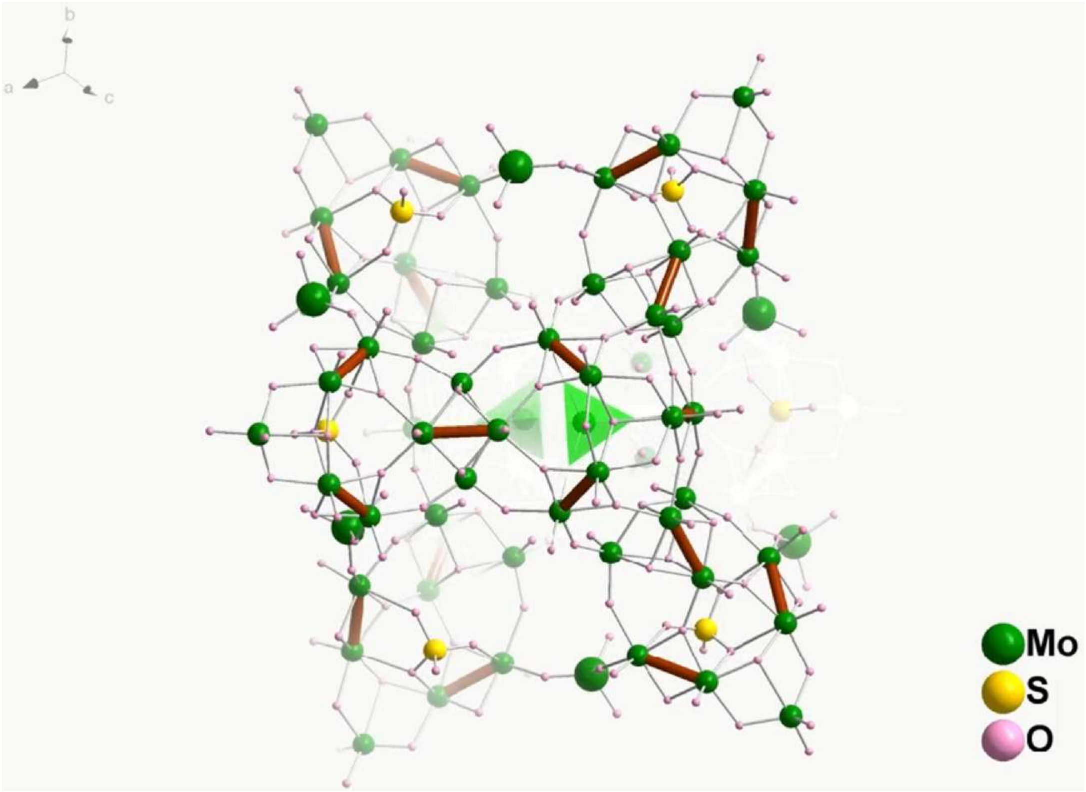

Video 2 A video clip is available online. Supplementary material related to this article can be found online at http://doi.org/10.1016/bs.adioch.2025.09.001.

wheels/ball all contain the $\{Mo_6\}$ pentagonal units, large Mo-red clusters are constructed from two primary BBs, coplanar $\{Mo^{V}_{6}\}$ and tripodal $\{Mo^{V}_{6}\}$, each containing three Mo^{V}-Mo^{V} bonded dimers (Fig. 2). These two BBs structurally correspond to two halves of the ε-Keggin isomer $\{Mo^{V}_{12}\}$,[69] representing the smallest and fully reduced Mo-red structure. The cubic $\{Mo_{64}\}$[67] (81 % reduced) features eight hexagonal $\{Mo^{V}_{6}\}$ subunits positioned at the cube vertices, complemented by four single Mo^{V} centres disordered over twelve edge centres, with structural stabilisation provided by six octahedrally arranged Ln^{III} ions and cubically positioned eight Ni^{II} ions (Fig. 2). The star $\{Mo_{70}\}$[67] (57 % reduced) consists of five $\{Mo_{10}\}$, each containing a tripodal $\{Mo^{V}_{6}\}$ core with a $\{Mo_3\}$ add-on group and an internal $\{MoO_4\}$ template, interconnected by five tetrahedral $\{Mo^{V}_{2}Mo_2\}$ linking units (Fig. 2). Lan et al.[36] achieved a breakthrough with the hydrothermal synthesis of the giant $\{Mo_{240}\}$ cluster which adopts a pentagonal dodecahedral framework constructed from twenty tripodal $\{Mo^{V}_{6}\}$ BBs bridged by thirty $\{Mo^{V}_{2}Mo_2\}$ connectors. This remarkable structure features an expansive 1.8 nm diameter cavity with twelve pentagonal windows and demonstrates a 75 % reduction level of its Mo centers. The $\{Mo_{70}\}$[67] star's core resembles one quarter of the $\{Mo_{240}\}$ architecture but with different templating groups under the tripodal $\{Mo^{V}_{6}\}$ BBs.[36] Lan et al.[70] subsequently extended the $\{Mo_{240}\}$ system with $\{MoO_4\}$ templates and obtained catalytically active derivatives $\{Mo_{250}\}$ and $\{Mo_{260}\}$, demonstrating POM assembly flexibility by reaction condition control.

Chen et al. reported the Mo-red cluster $\{Mo_{60}\}$[37] as containing exclusively Mo^{V} centres, but more details indicate the presence of twelve Mo^{IV} centres, evidenced by two characteristic Mo-Mo bonds (~2.6 Å) associated with each Mo^{IV} site (Fig. 2). These twelve Mo^{IV} centres assemble to form a structurally unprecedented ε-Keggin $\{Mo^{IV}_{12}\}$ cluster core exhibiting ideal tetrahedral symmetry, comprising four triangular $\{Mo^{IV}_{3}\}$ units (Fig. 2). This configuration represents the first experimental realization of a theoretically predicted but previously unobserved structural motif.[71] The hierarchical assembly of this cluster proceeds through two distinct encapsulation layers. First, four tripodal $\{Mo^{V}_{6}\}$ units align along the C_3-symmetric window directions of the ε-Keggin core. Subsequently, four additional tripodal $\{Mo^{V}_{6}\}$ units arrange themselves along the C_3-symmetric directions defined by the $\{Mo^{IV}_{3}\}$ triangles. The resulting $\{Mo^{IV}_{12}Mo^{V}_{48}\}$ architecture incorporates 60 Mo centres and possesses 72 reducing electrons, corresponding to an exceptional 120 % reduction level when calculated using conventional methods. This remarkable electronic configuration stems from the synergistic combination of the over-reduced ε-Keggin core with the surrounding $\{Mo_6^V\}$ units.

$\{Mo_{74}\}$[68] is a unique Mo red composed of two trefoil-shaped $\{Mo_{34}\}$ sections (Video 2). Each $\{Mo_{34}\}$ begins with a $\{MoO_4\}$-templated tripodal $\{Mo_6^V\}$ unit as the cluster core, which extends along the three gaps between its legs, each filled with a $\{Mo_2^VMo_2\}$ cubic bridging unit. These cubic units further connect to an external crippled tripodal $\{Mo_4^VMo_1\}$ templated by a $\{SO_4\}$. The two inherently unstable super-trefoil-shaped $\{Mo_{34}\}$ units are combined in a face-to-face yet staggered arrangement and stabilized by six $\{MoO_4\}$ units, which bridge the side edges of the trefoil blades.

Typical MB $\{Mo_{154}\}$, $\{Mo_{176}\}$, $\{Mo_{90}U_{10}\}$, and $\{Mo_{108}\}$ possess only delocalized reducing electrons, whereas Mo red species including $\{Mo_{240}\}$, $\{Mo_{70}\}$, $\{Mo_{64}\}$, $\{Mo_{60}\}$ and $\{Mo_{74}\}$ contain exclusively localized reducing electrons. In contrast, hybrids such as L-$\{Mo_{132}\}$, C-$\{Mo_{132}\}$ and $\{Mo_{172}\}$ feature both delocalized and localized reducing electrons, resulting in coloration distinct from typical blue or red. For example, C-$\{Mo_{132}\}$ has been reported to exhibit green hue. With the application of new synthetic method and the incorporation of organic ligands like phosphonates[66] in Mo-POM construction, it is anticipated that more new structural types of giant Mo-POMs, occupying the intermediate space between MB and Mo red, will be discovered in the near future.

3.3 Novel high nuclearity polyoxoniobates

Nb-POMs constitute a remarkable class of POM frameworks where niobium serves as the primary constituent alongside vanadium, tungsten, and other transition metals, forming structurally diverse and functionally versatile compounds.[72] These materials are distinguished by Nb's high +5 oxidation state and strong Lewis acidity, which endow them with unique catalytic and redox properties.[72,73] Compared to their Mo- and W-based counterparts, Nb-POMs present greater synthetic challenges: they are typically stable only under less acidic conditions, lack soluble precursors, require high pH for formation, and exhibit low reactivity. Consequently, Nb-POM chemistry remains less explored, with fewer reported studies. Structurally, Nb-POMs adopt well-defined architectures built from fundamental BBs, primarily Lindqvist-type clusters, interconnected by small linkers to form mixed-addenda species.[72] Their synthesis typically involves the acidic condensation of niobate precursors $[Nb_6O_{19}]^{8-}$ ($\{Nb_6\}$) with other transition metals under mildly acidic to neutral conditions, distinguishing them from Mo- or W-POMs that require strongly acidic conditions. Although Nb-POM chemistry has only developed significantly in the last two decades, recent advances have yielded numerous high nuclearity Nb-POMs constructed from well-defined BBs. Fig. 3.

Fig. 3 showcases representative Nb-POM recently discovered. The versatile $\{Nb_7\}$ BB, consisting of a Linqvest $\{Nb_6\}$[2] unit with an additional $\{Nb_1\}$ moiety, serves as a primary structure motif. Through equivalent $\{Nb_1\}$ linkers, multiple $\{Nb_7\}$ units can polymerize to form cyclic oligomers including trimeric $\{Nb_{24}\}$,[74,75] tetrameric $\{Nb_{32}\}$,[75,76] pentameric $\{Nb_{40}\}$,[77] and hexameric $\{Nb_{48}\}$.[78] These oligomers can further assemble into larger Nb-POM clusters through various combinations, incorporating with other transition metals. For instance one form of $\{Nb_{96}\}$ arises from the tetramerization of $\{Nb_{24}\}$,[75] while another originates from dimerization of $\{Nb_{48}\}$.[78] Similarly, $\{Nb_{192}\}$ results from the tetramerization of $\{Nb_{48}\}$.[78] Additional assemblies include $\{Nb_{120}\}$, formed from one

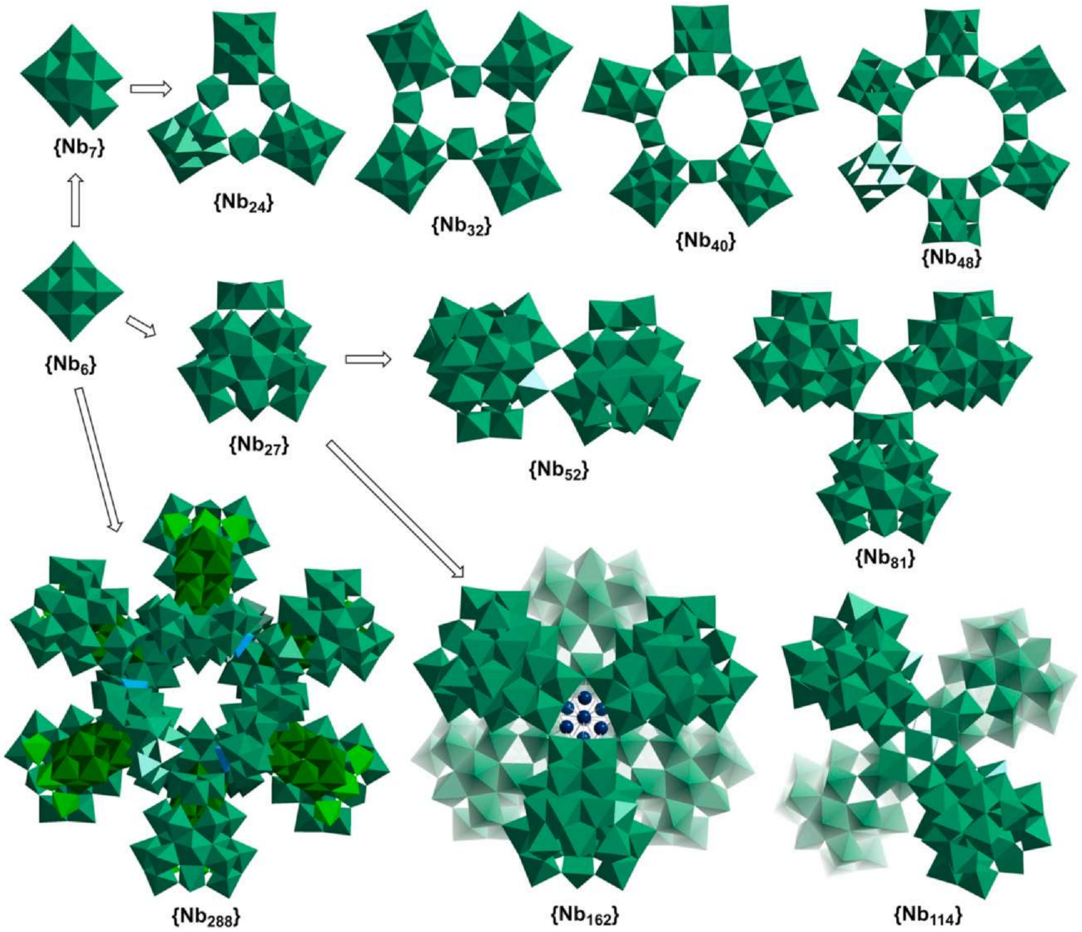

Fig. 3 Representative Nb-POM building blocks and clusters. Color scheme: Nb sea green in general, Ag dark teal. Exceptions for building blocks in $\{Nb_{288}\}$: $\{Nb_{17}\}$ sea green, $\{Nb_{10}\}$ green, $\{Nb_3\}$ bright green, $\{Nb_1\}$ turquoise.

$\{Nb_{48}\}$ plus three $\{Nb_{24}\}$ units, and $\{Nb_{128}\}$, composed of two $\{Nb_{40}\}$ and two $\{Nb_{24}\}$ units.[77] Another important BB is the stable and isolable $\{Nb_{27}\}$[79] cluster, which features a Keggin-like $\{Nb_{12}\}$ unit positioned atop a tripodal, bowl-shaped $\{Nb_{15}\}$ base. This $\{Nb_{27}\}$ BB exhibits remarkable polymerization capability,[80] forming dimeric $\{Nb_{52}\}$, trimeric $\{Nb_{81}\}$ and tetrameric $\{Nb_{114}\}$ structures through the loss or gain of small $\{Nb_1\}$ or $\{Nb_3\}$ units while retaining the fundamental $\{Nb_{27}\}$[79] framework. A particularly notable assembly, $\{Nb_{162}\}$,[81] consists of six $\{Nb_{27}\}$ encapsulating a $\{Ag_8\}$ core (Fig. 3).

The $\{Nb_{288}\}$ cluster,[82] containing 288 Nb atoms, currently stands for the largest and highest nuclearity Nb-POM reported, ranking as the second largest cluster among all classic POMs.[4] This remarkable structure adopts a unique windmill-like architecture composed of six nanoscale $\{Nb_{47}\}$ subunits interconnected through six additional $\{Nb_1\}$ linkers (Fig. 3). Each $\{Nb_{47}\}$ subunit itself exhibits a sophisticated ternary structure comprising three distinct components: $\{Nb_{17}\}$, $\{Nb_{10}\}$ and $\{Nb_3\}$ (Fig. 3). The unusual $\{Nb_{17}\}$ unit can be structurally described as a lacunary derivative of the $\{Nb_{27}\}$[79] cluster, while the $\{Nb_{10}\}$ unit results from the fusion of two Lindqvist anions through loss of two vertex Nb centres. The overall $\{Nb_{288}\}$ assembly possesses pseudo-six fold symmetry, with its principal rotational axis aligned with the six fold axis of the equatorial hexagonal ring formed by the six $\{Nb_1\}$ linkers. This elegant symmetrical arrangement highlights the sophisticated hierarchical organization characteristic of high-nuclearity Nb-POMs.

A groundbreaking advancement[83] in Nb-POM chemistry involves the isolation of a remarkable series of giant, all-inorganic core-shell cobalt Nb-POM clusters exhibiting diverse morphologies, nuclearities, and novel topologies, including $\{Co_{12}Nb_{38}\}$, $\{Co_{20}Nb_{34}\}$, $\{Co_{26}Nb_{36}\}$ and $\{Co_{33}Nb_{54}\}$ (Fig. 4). These molecular Co-Nb-POM clusters feature atomically precise architectures consisting of spinel-type cobalt oxide $Co^{II}Co_2^{III}O_4$ cores with different nuclearities encapsulated within niobium oxide shells. This successful synthesis of Co-Nb-POM clusters demonstrates a versatile and reproducible methodology for constructing rare, isolated spinel metal oxide systems with well-defined shell structures. The precise control over core-shell architecture in these molecular systems offers exceptional potential for applications in advanced materials science and molecular catalysis, particularly where defined metal oxide environments are crucial for catalytic performance.

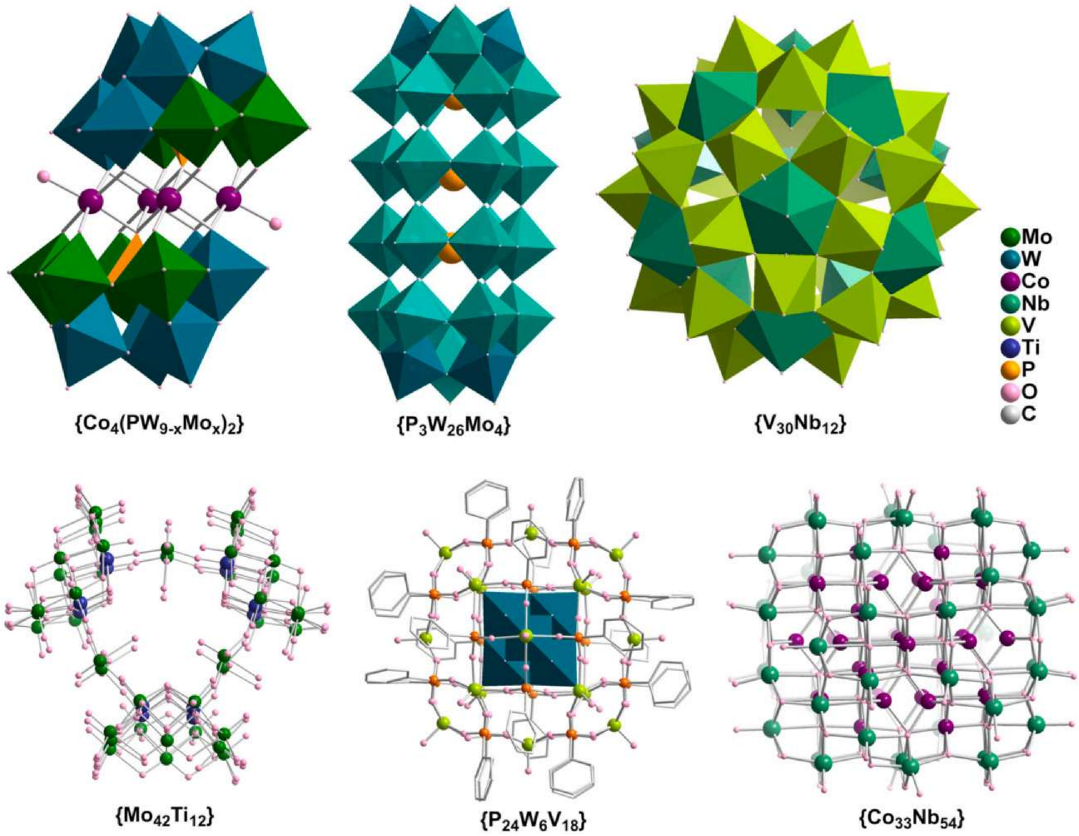
$\{Co_4(PW_{9-x}Mo_x)_2\}$ $\{P_3W_{26}Mo_4\}$ $\{V_{30}Nb_{12}\}$

$\{Mo_{42}Ti_{12}\}$ $\{P_{24}W_6V_{18}\}$ $\{Co_{33}Nb_{54}\}$

Fig. 4 Representative mixed metal POMs. In $\{Co_4(PW_{9-x}Mo_x)_2\}$, W and Mo are disordered over all sites but sea green sits have more W content while green sits have more Mo content.[84] In $\{P_3W_{26}Mo_4\}$, 4 Mo are distributed over all cyan sites.[86]

3.4 Maximizing POM functionalities by mixing metals

Incorporating mixed metals (e.g., Mo and W) into POMs combines their complementary properties, enhancing functionality. For instance, Mo-POMs exhibit higher reducibility and catalytic activity in oxidation reactions, whereas W-POMs provide stronger acidity and stability. Blending these metals fine-tunes redox behaviour, enabling optimized catalysis (e.g., for acid-driven or oxidative processes). Structurally, W enhances thermal and hydrolytic stability, while Mo introduces flexibility, facilitating novel architectures. Additionally, mixed metal POMs balance solubility - Mo enhances organic solvent compatibility, while W ensures aqueous stability – simplifying processing. Overall, strategic metal mixing tailors POMs for applications in catalysis, energy storage, materials science, and medicine by leveraging synergistic effects.[84,85] Cronin et al. demonstrated redox-active electrocatalyst tuning by doping Mo into the W framework of a $\{Co_4(PW_9)_2\}$ Weakley sandwich (see $\{Co_4(PW_{9-x}Mo_x)_2\}$ in Fig. 4).[84] This doping lowers the overpotential for the oxygen evolution reaction (OER), enabling efficient water oxidation without catalyst degradation. In another study, mixed redox-active pyramidal XO_3 heteroanions (X = P, As, Se) guided the assembly of multilayered POM cages (see e.g. $\{P_3W_{26}Mo_4\}$ in Fig. 4) driven by reduced Mo^V.[86] Ten mixed-valence Mo-W-POM clusters, templated by one to three XO_3 heteroanions, were synthesized, expanding the library of cylindrical POM structures with potential as linear molecular conductors. These clusters exhibit rapid dielectric relaxation (50–150 K), highlighting their promise for electronic materials. The $\{Mo_{42}Ti_{12}\}$[87] POM (Fig. 4), featuring surface peroxo groups, demonstrates exceptional photocatalytic activity in benzyl alcohol/benzaldehyde oxidation. Chi et al.[88] recently reported a unique fullerene-like Nb-V-POM cage, $\{V_{30}Nb_{12}\}$ (Fig. 4), by incorporating Nb into polyoxovanadate (V-POM). Its structure, assembled from 12 heterometallic $\{NbV_5\}$ pentagons with icosahedral symmetry, resembles C_{60}. Additionally, two core-shell mixed-metal POMs, $\{M_6V_{18}\}$ (M = Mo or W),[89] were synthesized using Lindqvist $\{M_6\}$ templates and phenylphosphonate ligands (see $\{P_{24}W_6V_{18}\}$ in Fig. 4). These compounds feature a nested octahedron@cube@octahedron architecture, offering insights into designing novel mixed-metal POMs with tuneable properties. The catalytically active $\{Ce^{IV}_{12}V_6\}$ cluster,[90] templated by sulfate vs sulfonate ligands, both adopts a cubane-like architecture with Ce^{IV} ions occupying the edges, vanadyl groups decorating the faces, and ligands positioned at the vertices. The incorporation of organic sulfonate ligands significantly enhances the cluster's solubility for homogeneous applications while simultaneously introducing porosity. This structural modification serves critical functions: increasing accessibility to catalytic sites, modulating the electronic environment of active centres, and boosting overall reactivity, as demonstrated by the selective oxidation of 2-chloroethyl ethyl sulfide. The strategic ligand functionalization fine-tunes cluster reactivity, providing valuable design principles for developing efficient redox-active and mixed-metal POM catalysts. Finally the $\{Co_{33}Nb_{54}\}$[83] discussed in previous section represents a good example of mixed metal oxide materials (Fig. 4).

3.5 Non-classical POMs

POM is classically defined as anionic molecular metal oxide. As the field has expanded beyond traditional Mo-, W-, V- and Nb-based systems, new classes such as polyoxopalladates (Pd-POMs)[91] and other anionic metal oxide clusters have been discovered and structurally characterized. A key feature of these non-classical POMs is their reliance on heteroanions for cluster formation, stabilization, and anionic charge. Pd-POM chemistry, developed over the past two decades, has yielded diverse structural types range from cubic $\{Pd_{12}\}$[92] to giant ring-shaped $\{Pd_{72}\}$ and $\{Pd_{84}\}$ clusters,[93] with intermediate architectures including star $\{Pd_{17}\}$[94] and dumbbell $\{Pd_{22}\}$[95] configuration. Recent advances include disk-like $\{Pd_{40}\}$[96] and Ce^{IV}-containing $\{Ce_8Pd_6\}$.[97] Similarly, uranium-based clusters represent another important class of non-classical POMs.[98,99] Nyman et al. recently reported uranyl-oxysulfate clusters $\{U_{70}\}$ and $\{U_{84}\}$,[100] whose assembly depends on solution acidity and counter-cations (lanthanides/transition metals). The hollow $\{U_{84}\}$ supercluster features 14 $\{U_6\}$ BBs arranged in cubic-close-packed networks via sulfate bridges, while wheel-shaped $\{U_{70}\}$ comprises 10 $\{U_7\}$ BBs stabilized by transition metals, exhibiting unique organic solubility for supramolecular applications. Notably, a toroidal zirconium oxysulfate cluster $\{Zr_{70}\}$[101] with a 1 nm inner cavity displays pseudo-10-fold rotational symmetry sharing structural motifs with the isostructural $\{U_{70}\}$. A remarkable example of non-classical POM assemblies is the stepwise formation of the $\{Ce_{70}\}$ ring cluster,[102,103] which consists of ten $\{Ce_7\}$ repeating BBs (Fig. 5) and is also an isostructure of $\{U_{70}\}$. This structure suggests simultaneous ring assembly and crystalline lattice organization during crystallization. While various metal counter-cations bridge rings via sulfates, their structural influence remains limited. However, ammonium cations uniquely induce spontaneous self-assembly of interlocked $\{Ce_{62}\}$ dimers[103] (Fig. 5), a novel inorganic motif. The $\{Ce_{62}\}$ cluster maintains the $\{Ce_{70}\}$ ring architecture but breaks and lacks eight Ce centres near the interlocking point. Both $\{Ce_{70}\}$ and $\{Ce_{62}\}$ exhibit lanthanide ion exchange, with the readily prepared ammonium salt of $\{Ce_{62}\}$ offering particular promise for redox-active and catalytic applications.

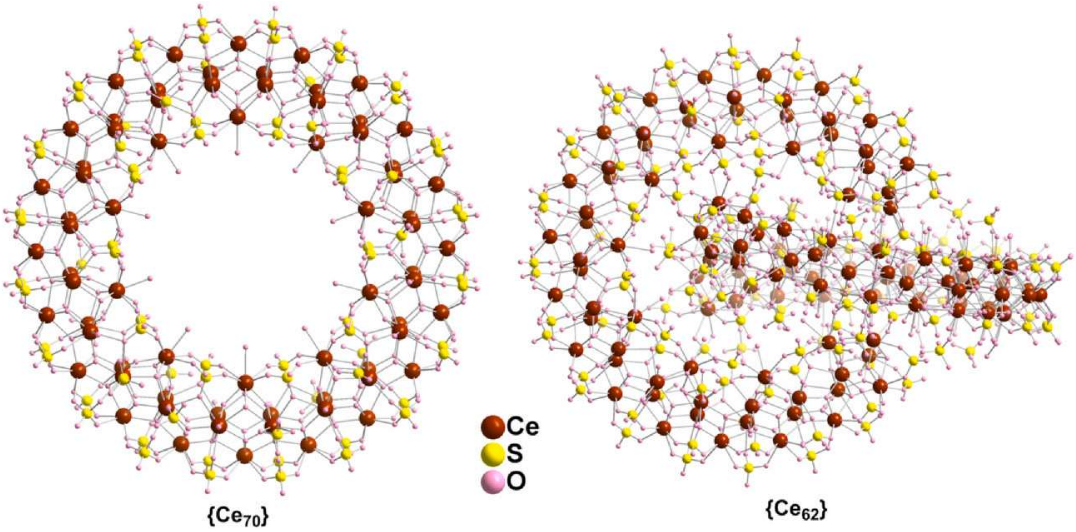

Fig. 5 Molecular structures of $\{Ce_{70}(SO_4)_{60}\}$ and $\{Ce_{62}(SO_4)_{58}\}$ interlocked dimer.

4. POM metal-organic hybrids

4.1 POM-mediated Ag clusters

Recent research on POM-stabilized silver clusters has gained significant attention. Unlike classical sol-gel derived silver nanoparticles with heterogeneous size distributions, POMs serve as versatile templates or ligands that enable the synthesis of atomically precise silver nanoclusters. The rigid, redox-active POM frameworks can encapsulate or bridge silver clusters, forming unique core-shell or cage-like architectures with tailored geometries. This synergy combines the plasmonic, catalytic, and luminescent properties of silver with the redox versatility and stability of POMs, yielding hybrid materials with applications in catalysis,[104] antimicrobial agents,[105] and energy storage.[106] The structural precision and multi-functionality of these Ag-POM systems establish them as a cutting-edge platform in nanotechnology and materials science.

POM-stabilized silver clusters can be classified into three categories: (1) Ag cluster-in-POM, (2) POM-templated Ag shell clusters, and (3) multi-layer alternating arrangements and infinite structures. The first type represents traditional structures where cluster sizes are constrained by POM cavity dimensions, as exemplified by $\{Ag_{12}@W_{76}\}$,[34] $\{Ag_7@(SiW_9)_3\}$,[107] $\{Ag_8@Nb_{162}\}$,[81] $\{Ag_{14}@(Sb_3W_{30})_2\}$,[108] $\{Ag_{24}@(Si_2W_{18}O_{66})_3\}$[109] and $\{Ag_8@(PNb_3W_{15})_6\}$.[110] Notably, the catalytically active $\{Ag_{30}@P_8W_{48}\}$ nanocluster[111,112] maintains exposed silver surfaces while achieving exceptional stability in both solution and solid states through encapsulation by $\{P_8W_{48}\}$. This system undergoes redox-induced structural transformations without agglomeration or decomposition. Similar POM-mediated clusters have been reported for other precious metals including Au[113] and Cu.[114]

Recent research has primarily focused on the second and third categories, which typically employ anionic organic ligands (carboxylates, alkynates, and thiolates etc.) for surface stabilization and charge balance. A remarkable triple core-shell structure $\{Ag_{10}@(W_7)_2@Ag_{74}\}$ (Fig. 6) features an inner $\{Ag_{10}\}$ core wrapped by two crescent-shaped $\{W_7\}$ units, further enclosed within a rugby ball-shaped $\{Ag_{74}\}$ shell, with external stabilization by Pr^iS^-, $Pr^nCO_2^-$ and $PhCO_2^-$ ligands.[115] Structural variations at the poles and steric effects of $Pr^nCO_2^-/PhCO_2^-$ give rise to two isomers: flat-headed and cuspidal prolate spheres. Ligand exchange studies revealed distinct preferences between isomers, demonstrating how organic ligands can induce shell reorganization beyond simple surface modification. Sun et al. reported $\{P_5W_{30}@Ag_{43}\}$ cluster stabilized by alkynate ligands

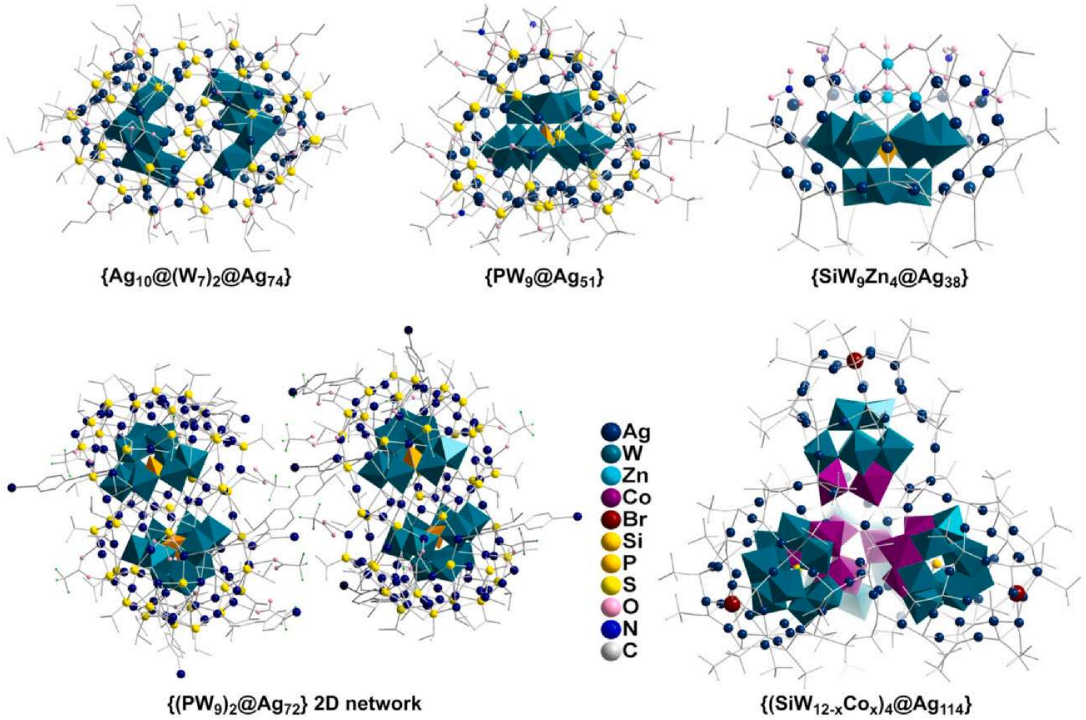

Fig. 6 Representative POM-mediated Ag cluster structures.

and provided a comprehensive compilation of early POM-templated Ag shell clusters in the references therein.[116] More recent advances include lacunary Keggin POM templated structures: single-pod $\{PW_9@Ag_{51}\}$ clusters[117] fuse via 4,4'-bipyridine or 1,4-bis(4-pyridinylmethyl)piperazine linkers to form double-pod $\{(PW_9)_2@Ag_{72}\}$ assemblies, yielding 2D layer or 3D framework, respectively. This represents a paradigm shift from empirical approaches to designed synthesis strategies. A number of example show that open-shell clusters can be obtained by templation from transition-metal-substituted POMs, for instance, the cluster $\{SiW_9Zn_4@Ag_{38}\}$ (Fig. 6), where W=O sites bind Ag^I ions while the Zn sites (with acetate/hydroxyl ligands) create structural windows.[118] Yang et al.[104] reported the largest known Ag cluster $\{Ag_{114}\}$ templated by a supertetrahedral $\{(SiW_{12-x}Co_x)_4\}$ aggregate, which catalyzes light-driven CO_2 reduction when coupled with $[Ru(bpy)_3]Cl_2$ photosensitizer and triethanolamine sacrificial donor. Notably, the structural diversity extends beyond closed-shell architectures.

4.2 Organic ligand directed assembly of giant POM-based cages

Giant cluster cages are highly appealing due to their intricate architecture, which resembles biological macromolecules. POMs serve as ideal molecular models for studying and mimicking complex nanoclusters, combining tuneable geometry and chemistry with the functional versatility of metal oxides. These properties make them exceptional nanoscale systems for applications in catalysis, energy storage, and biomedicine.

V-POMs offer distinct advantages for effectively constructing hybrid POM clusters, as their modular motifs, such as trigonal $\{V_3\}$, square $\{V_4\}$, pentagonal $\{V_5\}$ and hexagonal $\{V_6\}$, provide well-defined binding sites for organic ligands, enabling predictable assembly. Rigid multi-dentate O,N-donor ligands with high affinity for vanadium ions further facilitate the formation of highly symmetrical cages.[119,120] This approach has yielded high-nuclearity aggregates with tetrahedral, octahedral, and cubic topologies.[121] Recent breakthroughs include fullerene-like cages constructed from sulfate-templated pentagonal $\{V_5S\}$ BBs and benzenetricarboxylate (BTC).[122] The icosahedral $\{V_{60}\}$ cage, composed of 12 pentagonal $\{V_5S\}$ units bridged by 20 BTC spacers (Fig. 7), exemplifies this architecture. By modifying the $\{V_5\}$ BB to V-centred $\{V_6\}$ or Mo-centred $\{MoV_5\}$ units, two isomorphic cages, $\{V_{72}\}$ and $\{V_{60}Mo_{12}\}$ (Fig. 7) were also isolated. An intermediate structure, $\{V_{66}\}$, containing both $\{V_5\}$ and $\{V_6\}$ BBs,

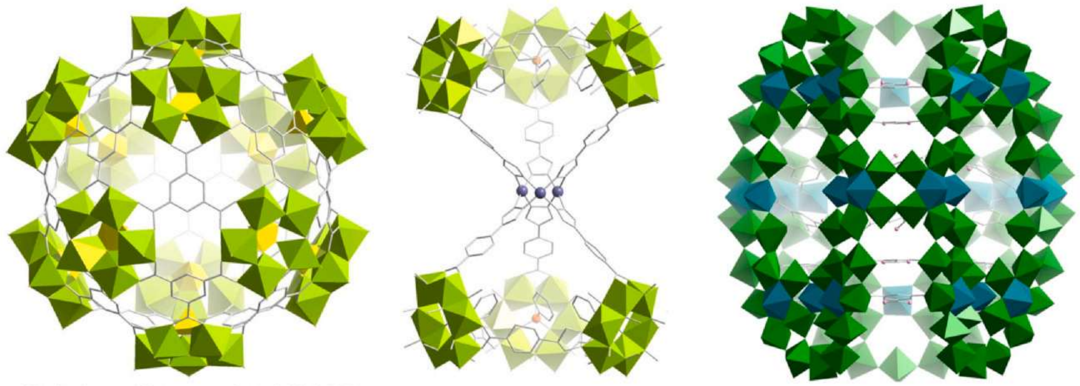

$\{V_{60}\}$ - by sulfate-templated $\{V_5\}$ BB

$\{V_{36}Pd_3\}$

$\{Mo_{126}W_{30}\}$ side view

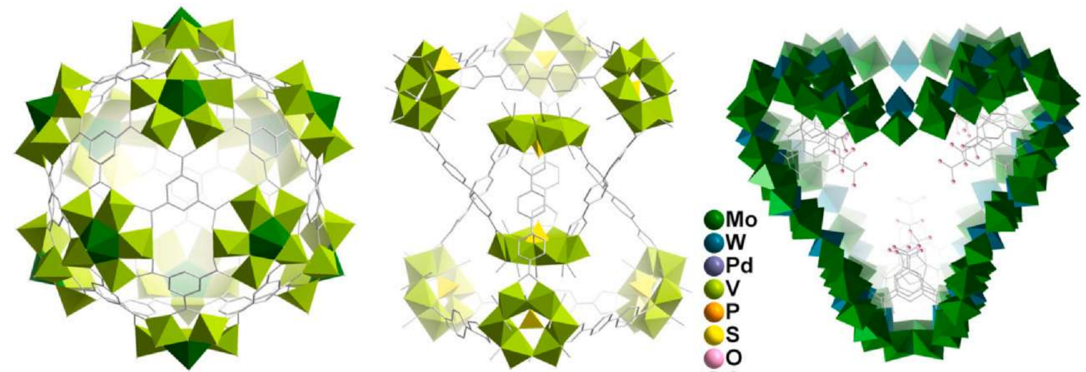

$\{V_{60}Mo_{12}\}$ - by Mo centred $\{MoV_5\}$ BB

$\{V_{24}\}$ catenated dimer

$\{Mo_{126}W_{30}\}$ top view

Fig. 7 Representative organic ligand directed giant POM-based cages: $\{V_{60}\}$ and $\{V_{60}Mo_{12}\}$[122]; $\{V_{36}Pd_3\}$ and $\{V_{24}\}$ dimer[123]; $\{Mo_{126}W_{30}\}$.[124]

was crystallized, demonstrating the complexity of this self-assembly system. These clusters represent the highest nuclearity V-POM structures reported to date. One other outstanding demonstration of organic ligand-directed V-POM assembly involves the construction of tetrahedral pyrgo[2]cage molecular architectures and interlocked catenanes based on hexagonal $\{V_6\}$ BBs bridged by organic ligands.[123] Three key synthetic strategies enabled these structures: (1) vertex reconstruction, where sulfate-centered $\{V_6S\}$ vertices are replaced by phenylphosphonate-centered $\{V_6P\}$ vertices to create cages with tuneable cavity dimensions; (2) exogenous vertex incorporation, substituting one $\{V_6\}$ vertex with a shared $\{Pd_3\}$ vertex to form pyrgo[2]cage molecule $\{V_{36}Pd_3\}$ (Fig. 7); and (3) polyhedral interlocking, achieved by precisely modulating organic linker lengths and intermolecular interactions to assemble tetrahedral monomers into hourglass-shaped $\{V_{24}\}$ catenated dimers (Fig. 7). Through this synergistic combination of covalent and non-covalent interactions, the approach yields novel structural types exhibiting unique properties, such as selective NH_3 gas adsorption.

Suzuki et al. have established another notable class of POM-based cage assemblies using lacunary POMs.[125] Keggin-type lacunary POMs like $\{PMo_9\}$[126] and $\{SiW_{10}\}$[127] provide structurally defined coordination sites with versatile geometries while maintaining tuneable properties. Particularly useful are pyridine-functionalized lacunary Mo-POMs such as $\{PMo_9O_{31}(py)_3\}$[126] which offer organic solubility and serve as excellent synthetic precursors for constructing POM-organic hybrid structures. Through ligand exchange reactions, these $\{PMo_9\}$ BBs can form dimeric cages when bridged by 4,4'-bipyridyl spacers or tetrameric assemblies when connected by cofacial porphyrin ligands. Remarkably, these resulting structures exhibit exceptional photocatalytic performance, demonstrating highly efficient and durable visible-light-responsive activity for aerobic oxidation reactions.[127] Fang et al.[124] presented the assembly of giant mixed-metal $\{Mo_{126}W_{30}\}$ POM cages templated by π-conjugated planar polycarboxylate ligands. These architectures feature inorganic shells incorporating 18 stacked aromatic carboxylates, such as BTC (Fig. 7) or 5-nitroisophthalate, stabilized by extensive π-π interactions. The cages exhibit remarkable solution stability, and their embedded aromatic templates can be post-synthetically exchanged with aliphatic dicarboxylates. This strategy enables precise endo-functionalization of the cage cavities, opening avenues to explore confined reactivity and host-guest chemistry. The work represents a significant advance in constructing hybrid organic-inorganic systems through controlled supramolecular templating.

4.3 POM embedded MOF

Metal-organic frameworks (MOFs) embedded with POMs (POMOFs) represent a highly versatile class of hybrid materials that synergistically combine the unique properties of both components, leading to enhanced performance across various applications.[120] MOFs provide a highly porous, tuneable, and structurally robust framework, while POMs contribute strong acidity, redox activity, and catalytic functionality.[128,129] One of the most significant advantages of POMOF composites is their superior catalytic performance, where POMs act as active sites for acid-catalyzed, oxidation, and reduction reactions, while the MOF matrix prevents POM aggregation and leaching, ensuring recyclability and stability.[130] This makes them ideal for heterogeneous catalysis in industrial processes, such as fuel desulfurization, fine chemical synthesis, and biomass conversion. Additionally, the confined pore environment of MOFs enables size- and shape-selective catalysis, enhancing reaction specificity. A remarkable example is $\{(PW_{12})_6@(Cu_{12}BTC_8)\}$,[128] in which Keggin-type POM $\{PW_{12}\}$ clusters are encapsulated in Cu-BTC MOF structures (Fig. 8). There are large cavities with number and location comparable to those of POM sites in the structure, providing enhanced accessibility for substrate and displaying excellent catalytic performance. Also a series of POMOFs based on metalloporphyrins ligands were constructed for photo- and electrocatalytic CO_2 reductions.[131]

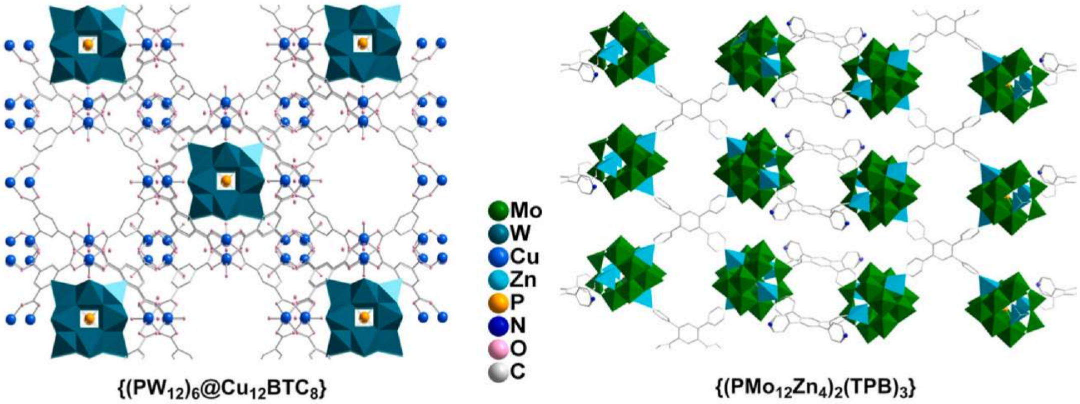

Fig. 8 Representative POMOFs. $\{(PW_{12})_6@(Cu_{12}BTC_8)\}$[128]: Keggin-type POM $\{PW_{12}\}$ clusters are captured in Cu-BTC MOF structures; Note large cavities with number and location comparable to those of POM $\{PW_{12}\}$ clusters in the structure. $\{(PMo_{12}Zn_4)_2(TPB)_3\}$[138] based on Zn-added ε-Keggin POM $\{PMo_{12}\}$ and 1,2,4,5-tetrakis (4-pyridyl)benzene (TPB) ligand.

Beyond catalysis, POMOF hybrids exhibit exceptional redox properties, making them promising for energy storage applications, including batteries and supercapacitors, where POMs provide multi-electron redox activity and MOFs ensure structural integrity.[132–134] Their high proton conductivity also renders them suitable for fuel cell membranes.[15,135,136] In environmental applications, these composites excel in gas and ion adsorption and separation, particularly for CO_2 capture and hydrogen storage, due to their adjustable porosity and POM-enhanced binding sites.[137] Furthermore, their photocatalytic capabilities are leveraged for water splitting and pollutant degradation, where POMs act as efficient photosensitizers within the MOF scaffold. Notable examples include that POMOF $\{(PMo_{12}Zn_4)_2(TPB)_3\}$[138] based on ε-Keggin POM $\{PMo_{12}\}$ incorporated in Zn-polypyridyl MOF (Fig. 8) was designed for uranium capture.[138]

The integration of POMs into MOFs also expands their utility in sensing and biomedical applications. The redox-active and optically responsive nature of POMs, combined with MOF porosity, allows for selective detection of toxic chemicals, explosives, or biomolecules.[139] In drug delivery, POMOF systems enable controlled release mechanisms, with some POMs contributing additional therapeutic effects, such as antimicrobial or anticancer activity. The stability of these hybrids under harsh conditions - thermal, chemical, and aqueous – further broadens their applicability compared to standalone POMs or MOFs.[140]

5. Self-organisation to high order materials

POM clusters with atomic-level precision are promising candidates for constructing functional nanomaterials via self-organisation. Their self-assembly can be governed by non-covalent interactions, allowing precise control of POM-based architectures at the single-cluster levels. Guided by supramolecular force, the self-assembly process bring together multiple components to form stable aggregates. A notable example is the $\{Mo_{154}\}$-based host-guest composite $\{(Mo_6@\gamma\text{-CD})_2@Mo_{154}\}$, comprising five hierarchically organized components held together by noncovalent interactions.[141] Structure analysis reveals that the $\{Mo_{154}\}$ wheel accommodates two supramolecular adducts formed by the symmetric encapsulation of Lindqvist-type $\{Mo_6\}$ anions within γ-cyclodextrin (γ-CD) units (Fig. 9). Using amino acids like L-ornithine (Orn) as a structure-directing reagents, diverse complex systems

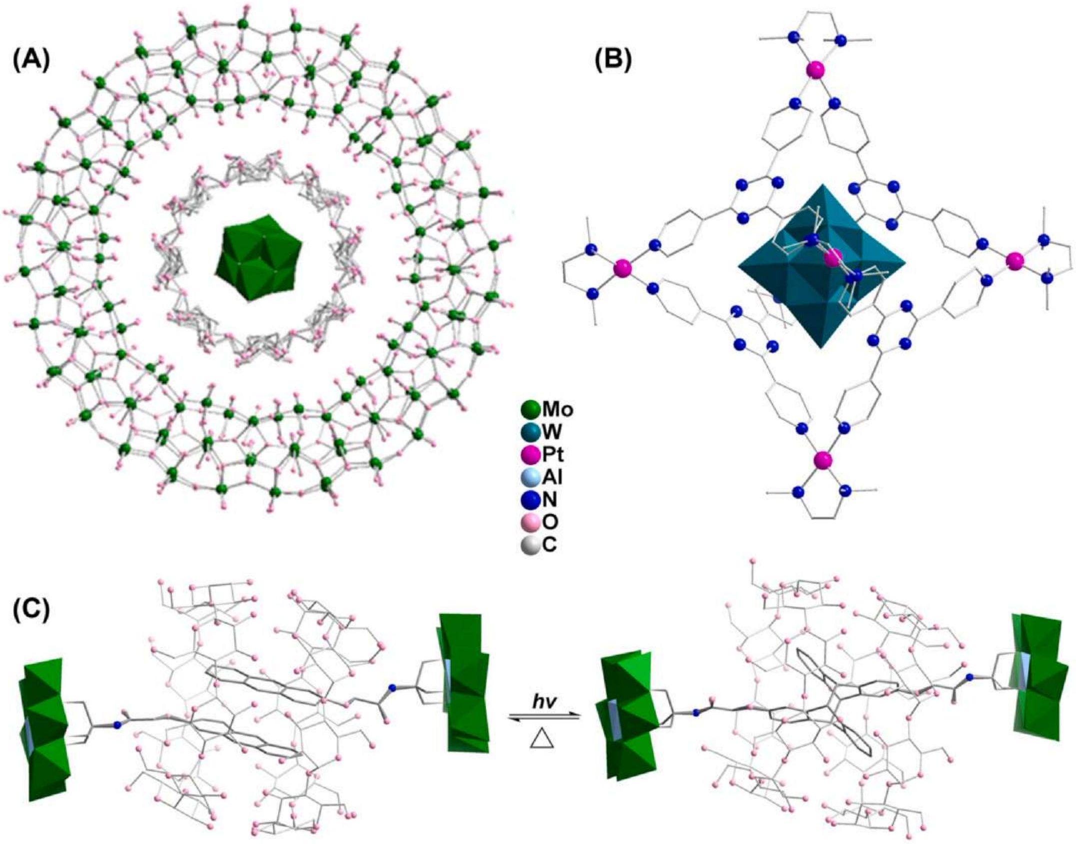

Fig. 9 (A) {$(Mo_6@\gamma\text{-}CD)_2@Mo_{154}$}[141]; (B) {$W_6@Pt_6L_4$} (L = 2,4,6-tris(4-pyridyl)-1,3,5-triazine)[142]; (C) Photo-responsive feature demonstrated by the *pseudo*-[4]rotaxanes based on double γ-CD wheels and a pair of Anderson-type {$AlMo_6$}-anthracene axles.[143]

such as {$Mo_8@Mo_{124}Ce_4(Orn)_6$}, {$Mo_{17}@Mo_{150}Ce_2(Orn)_6$}, {$PMo_{12}@Mo_{150}Ce_2(Orn)_6$} and {$Mo_{36}@Mo_{150}(Orn)_6$} have been assembled – varying in both host and guest POM sizes and types.[58] In another example, Lindqvist-type {Mo_6} and {W_6} anions are encapsulated in {Pt_6L_4} coordination cages (Fig. 9) to enhance their stability and catalysis efficiency (L = 2,4,6-tris(4-pyridyl)−1,3,5-triazine).[142] Additionally, *pseudo*-[4]rotaxanes composed of double γ-CD wheels and a pair of Anderson-type {$AlMo_6$}-anthracene axles exhibit photo-responsive properties, paving the way for multifunctional molecular machines (Fig. 9).[143] These key studies collectively demonstrate the principles of self-assembly and provide practical strategies for designing complex multicomponent materials using the elegant simplicity of the non-covalent chemistry, Fig. 9.

At nanometer scale, POM clusters in aqueous solution tend to spontaneously self-organize into stable, uniform, hollow spherical assemblies known as “blackberry” structures.[144,145] This formation is primarily driven by counterion-mediated electrostatic attractions and hydrogen bonding, distinct from van der Waals forces, hydrophobic interactions, or covalent chemical reactions.[146,147] One prominent example involves the $\{Mo_{154}\}$ cluster, which exhibits strong affinity for a nonionic surfactant n-octyl-β-glucoside. This interaction yielded well-defined discrete species such as vesicles, large lamellar aggregates, or nanosheets.[148] In another case, a covalently connected POM-β-cyclodextrin (β-CD) organic–inorganic hybrid serves as a water-dispersible host. It interacts at the water/oil interface with guest molecules dissolved in the oil phase via electrostatic or host–guest interactions, forming POM-surfactant composites responsive to pH, redox conditions, and competitive guest binding.[25] Additionally, a system comprising Keggin-type $\{PMo_{12}\}$ clusters paired with protonated amine-terminated polydimethylsiloxane cations demonstrates reversible emulsification behaviour in POM-organic polymer composites, offering promising avenues for the design of functional materials.[149]

Wang et al. conducted a series of studies on sub-1 nm materials (SNMs) derived from POMs in solid state, focusing on their synthesis, distinctive properties, and potential applications.[150] SNMs, characterized by feature sizes approaching 1 nm (e.g., the diameter of nanowires and thickness of monolayer), exhibit behaviors that differ significantly from both molecular and conventional nanomaterials.[151] This is primarily due to their exceptionally high surface atom ratios and unsaturated coordination environments, which give rise to phenomena such as surface atom rearrangement, electron delocalization, and intrinsic chirality.[152,153] The synthesis of SNMs involves strategies such as oriented nucleation, anisotropic cluster assembly, and cluster-nucleus co-assembly, enabling precise structural control.[154] Notable properties of SNMs include polymer-like flexibility and processability, stabilization of metastable phases, formation of high-entropy materials at relatively low temperatures, and enhanced catalytic performance driven by electron delocalization.[155,156]

POMs can covalently or non-covalently link to a variety of biomolecules, including amino acids, peptides, porphyrins, sugars, and vitamins, to form functional hybrid materials.[157,158] Such hybrids often exhibit enhanced biocompatibility, catalytic efficiency, and selectivity, making them promising candidates for biomedical and environmental applications.[159–162] Synthetic approaches include supramolecular assembly via electrostatic interactions with organic cations, as well as covalent or post-synthetic functionalization methods such as "click" chemistry, enabling the construction of complex architectures.[23,24]

6. Perspective

Polyoxometalate chemistry has rapidly evolved from a niche area within inorganic research to a central pillar of materials science. Over the past decade, the field has witnessed an explosion of novel POM structures and POM-based composites, with applications spanning catalysis, energy storage, and biomedicine. These molecular metal oxides represent one of the most versatile classes of inorganic compounds, owing to their tuneable composition, structural diversity, and multifunctionality. Recent advances have enabled the design of POM hybrids with finely adjustable porosity, catalytic activity, and stability, making them invaluable for sustainable and high-performance technologies. Their inherent design flexibility allows for precise tailoring of properties, positioning POMs as promising candidates for next-generation functional materials.

Looking ahead, the future of POM self-assembly and self-organisation will be shaped by innovations in synthetic methodologies, structural exploration, and application-driven design. Key directions include the discovery of novel clusters with unique architectures, such as high-nuclearity aggregates, mixed-metal systems, and organically functionalized derivatives. Enhanced control over solution-phase and solid-state synthesis, including pH-dependent, solvent-mediated, and template-directed assembly, will be critical for expanding the structural landscape. The integration of POMs with organic ligands, polymers, and nanoparticles to form hybrid frameworks is expected to unlock new functionalities. However, challenges persist, particularly in stabilizing large aggregates, elucidating assembly mechanisms, and understanding speciation in complex environments. Addressing these issues will require the development of generalized synthetic strategies and atomic-level control over composition and structure.

Artificial intelligence (AI) is poised to play a transformative role in accelerating POM research.[163] By leveraging machine learning and computational tools, AI can predict novel structures, optimize functional properties, and guide synthetic pathways. Techniques such as generative models, graph neural networks, and high-throughput screening offer powerful means to navigate vast chemical spaces and identify optimal POM compositions.[162,164,165] Moreover, AI can simulate reaction mechanisms and integrate literature data to minimize experimental trial-and-error. As we move forward, the convergence of AI-driven design,[166] advanced characterization techniques,[167] and sustainable synthesis approaches[21,168] will catalyze remarkable discoveries in POM chemistry. This synergy will not only deepen our understanding of self-assembly processes but also pave the way for the rational design of multifunctional materials tailored for emerging technological challenges.

Appendix. Supporting information

Supplementary data associated with this article can be found in the online version at http://doi.org/10.1016/bs.adioch.2025.09.001.

References

1. Berzelius, J. J. *Poggendorff's Ann. Phys. Chem.* **1826,** *6* 369-369.
2. Lindqvist, I. *Ark. Kemi.* **1953,** *5*, 247–250.
3. Keggin, J. F. *Proc. R. Soc. Lond. A* **1934,** *144*, 0075–0100.
4. Muller, A.; Beckmann, E.; Bogge, H.; Schmidtmann, M.; Dress, A. Angew. *Chem. Int. Ed.* **2002,** *41*, 1162–1167.
5. Liu, L.-L.; Wang, L.; Xiao, X.-Y.; Yang, P.; Zhao, J. Kortz. *U. Coord. Chem. Rev.* **2024,** *506*, 215687.
6. Colliard, I.; Lee, J. R. I.; Colla, C. A., et al. *Nat. Chem.* **2022,** *14*, 1357–1366.
7. Amthor, S.; Knoll, S.; Heiland, M., et al. *Nat. Chem.* **2022,** *14*, 321–327.
8. D'Cruz, B.; Amin, M. O. Al-Hetlani. *E. Ind. & Eng. Chem. Res.* **2021,** *60*, 10960–10977.
9. Perry, I. B.; Brewer, T. F.; Sarver, P. J.; Schultz, D. M.; DiRocco, D. A.; MacMillan, D. W. C. *Nature* **2018,** *560*, 70–75.
10. Blasco-Ahicart, M.; Soriano-Lopez, J.; Carbo, J. J.; Poblet, J. M.; Galan-Mascaros, J. R. *Nat. Chem.* **2018,** *10*, 24–30.
11. Li, N.; Liu, J.; Dong, B.-X.; Lan, Y.-Q. *Angew. Chem. Int. Ed.* **2020,** *59*, 20779–20793.
12. Gobbo, P.; Tian, L.; Kumar, B. V. V. S. P., et al. *Nat. Commun.* **2020,** *11*, 41.
13. Dubal, D. P.; Chodankar, N. R.; Kim, D.-H.; Gomez-Romero, P. *Chem. Soc. Rev.* **2018,** *47*, 2065–2129.
14. Wang, C.; Duan, X.; Jiang, Y., et al. *Adv. Mater.* **2025,** *37*, 2500114.
15. Cheng, D.; Li, K.; Zang, H. Chen. *J. Energy & Environ. Mater.* **2023,** *6*, e12341.
16. Zhang, H.; Li, A.; Li, K., et al. *Nature* **2023,** *616*, 482–487.
17. Lei, J.; Fan, X.-X.; Liu, T., et al. *Nat. Commun.* **2022,** *13*, 202.
18. Kolesov, V. A.; Fuentes-Hernandez, C.; Chou, W.-F., et al. *Nat. Mater.* **2017,** *16*, 474–481.
19. Xie, X.; Li, R.; Qiao, Y., et al. *Nat. Commun.* **2025,** *16*, 4872.
20. Miras, H. N.; Long, D.-L.; Cronin, L. *Adv. Inorg. Chem.* **2017,** *69*, 1–28.
21. Ma, X.-Q.; Xiao, H.-P.; Chen, Y.; Lai, Q.-S.; Li, X.-X.; Zheng, S.-T. *Coord. Chem. Rev.* **2024,** *510*, 215818.
22. Liu, J.-X.; Zhang, X.-B.; Li, Y.-L.; Huang, S.-L.; Yang, G.-Y. Coord. *Chem. Rev.* **2020,** *414*, 213260.
23. Lentink, S.; Marcano, D. E. S. E.; Moussawi, M. A., et al. *Angew. Chem. Int. Ed.* **2023,** *62*, e202303817.
24. Budych, M. J. W.; Staszak, K.; Bajek, A., et al. *Coord. Chem. Rev.* **2023,** *493*, 215306.
25. Xia, Z.; Lin, C.-G.; Yang, Y., et al. *Angew. Chem. Int. Ed.* **2022,** e202203741.
26. McNulty, R. C.; Penston, K.; Amin, S. S., et al. *Chem. Int. Ed.* **2023,** *62*, e202216066.
27. Yang, M.; Li, H.; Wang, J., et al. *Nat. Energy* **2024,** *9*, 143–153.
28. Zhu, M.; Xu, B.; Chen, T.; Zhang, J.; Sun, W. *Adv. Funct. Mater.* **2024,** *34*, 2406840.
29. Jiang, W.; Fan, B.; Kong, L., et al. *Angew. Chem. Int. Ed.* **2025,** *64*, e202507273.

30. Muller, A.; Meyer, J.; Krickemeyer, E.; Diemann, E. Angew. *Chem. Int. Ed. Engl.* **1996,** *35*, 1206–1208.
31. Alizadeh, M. H.; Harmalker, S. P.; Jeannin, Y.; Martinfrere, J.; Pope, M. T. *J. Am. Chem. Soc.* **1985,** *107*, 2662–2669.
32. Misra, A.; Kozma, K.; Streb, C.; Nyman, M. *Angew. Chem. Int. Ed.* **2020,** *59*, 596–612.
33. Long, D.-L.; Tsunashima, R.; Cronin, L. *Angew. Chem. Int. Ed.* **2010,** *49*, 1736–1758.
34. Zhan, C.; Cameron, J. M.; Gao, J.; Purcell, J. W.; Long, D.-L.; Cronin, L. *Angew. Chem. Int. Ed.* **2014,** *53*, 10362–10366.
35. Ribo, E. G.; Bell, N. L.; Xuan, W., et al. *Am. Chem. Soc.* **2020,** *142*, 17508–17514.
36. Lin, J.; Li, N.; Yang, S., et al. *J. Am. Chem. Soc.* **2020,** *142*, 13982–13988.
37. Li, X.-X.; Ji, T.; Gao, J.-Y., et al. *Chem. Sci.* **2022,** *13*, 4573–4580.
38. Dipalo, M. C.; Yu, B.; Cheng, X., et al. *Nanoscale* **2024,** *16*, 8900–8906.
39. Spillane, S.; Sharma, R.; Zavras, A., et al. *Angew. Chem. Int. Ed.* **2017,** *56*, 8568–8572.
40. Martin, S.; Takashima, Y.; Lin, C.-G.; Song, Y.-F.; Miras, H. N.; Cronin, L. *Inorg. Chem.* **2019,** *58*, 4110–4116.
41. Liu, G.; Huang, X.; Li, Y., et al. *Chin. J. Chem.* **2025,** *43*, 1968–1976.
42. Ng, M. T.-K.; Bell, N. L.; Long, D.-L.; Cronin, L. *J. Am. Chem. Soc.* **2021,** *143*, 20059–20063.
43. Priso, G. M.; Haouas, M.; Leclerc, N.; Falaise, C.; Cadot, E. *Angew. Chem. Int. Ed.* **2023,** *62*, e202312457.
44. Falaise, C.; Priso, G. M.; Leclerc, N.; Haouas, M.; Cadot, E. *Inorg. Chem.* **2023**, 2494–2502.
45. Xu, S.-Y.; Shi, W.; Huang, J.-R., et al. *Angew. Chem. Int. Ed.* **2024,** *63*, e202406223.
46. Repp, S.; Remmers, M.; Rein, A. S. J., et al. *Nat. Commun.* **2023,** *14*, 5563.
47. Pascual-Borras, M.; Arca, E.; Yoshikawa, H.; Penfold, T.; Waddell, P. G.; Errington, R. J. J. *Am. Chem. Soc.* **2024,** *146*, 26485–26496.
48. Long, D.-L.; Cronin, L. *Adv. Inorg. Chem.* **2021,** *78*, 227–267.
49. Muller, A.; Sarkar, S.; Shah, S. Q. N., et al. *Angew. Chem. Int. Ed.* **1999,** *38*, 3238–3241.
50. Muller, A.; Shah, S. Q. N.; Bogge, H., et al. *Angew. Chem. Int. Ed.* **2000,** *39*, 1614–1616.
51. Muller, A.; Krickemeyer, E.; Bogge, H., et al. *Angew. Chem. Int. Ed.* **1998,** *37*, 1220–1223.
52. Jiang, C. C.; Wei, Y. G.; Liu, Q.; Zhang, S. W.; Shao, M. C.; Tang, Y. Q. *Chem. Commun.* **1998**, 1937–1938.
53. Muller, A.; Shah, S. Q. N.; Bogge, H.; Schmidtmann, M. *Nature* **1999,** *397*, 48–50.
54. Cronin, L.; Beugholt, C.; Krickemeyer, E., et al. *Angew. Chem. Int. Ed.* **2002,** *41*, 2805–2808.
55. She, S.; Xuan, W.; Bell, N. L., et al. *Chem. Sci.* **2021,** *12*, 2427–2432.
56. Miras, H. N.; Mathis, C.; Xuan, W.; Long, D.-L.; Pow, R.; Cronin, L. *Proc. Natl. Acad. Sci. USA* **2020,** *117*, 10699–10705.
57. Xuan, W.; Pow, R.; Watfa, N., et al. *J. Am. Chem. Soc.* **2019,** *141*, 1242–1250.
58. Xuan, W.; Pow, R.; Zheng, Q.; Watfa, N.; Long, D.-L.; Cronin, L. *Angew. Chem. Int. Ed.* **2019,** *58*, 10867–10872.
59. Duros, V.; Grizou, J.; Xuan, W., et al. *Angew. Chem. Int. Ed.* **2017,** *56*, 10815–10820.
60. Liu, J.; Jiang, N.; Lin, J.-M., et al. *Angew. Chem. Int. Ed.* **2023,** *62*, e202304728.
61. Li, X.-X.; Li, C.-H.; Hou, M.-J., et al. *Nat. Commun.* **2023,** *14*, 5025.
62. Felton, D. E.; Smith, K. R.; Poole, N. A., et al. *Chem. Eur. J.* **2024,** *30*, e202400678.

63. Lakhanpal, V.; Guillen-Soler, M.; Vila-Nadal, L.; Long, D.-L.; Cronin, L. *J. Am. Chem. Soc.* **2025,** *147*, 10579–10586.
64. Zeng, H.-M.; Cheng, M.; Xuan, W.; Wei, Y. *Inorg. Chem.* **2024,** *64*, 67–72.
65. Hou, M.; Li, X.; Zhao, C., et al. *Adv. Funct. Mater* **2025**, e10454.
66. Cheng, M.; Zhang, D.; Liu, Y., et al. *CCS Chem.* **2025,** *7*, 2284–2292.
67. Ribo, E. G.; Bell, N. L.; Long, D.-L., et al. *Angew. Chem. Int. Ed.* **2022,** *61*, e202201672.
68. Liu, S.-Y.; Li, X.-X.; Chen, W.-C., et al. *Sci. China-Chemistry* **2024,** *67*, 862–868.
69. Müller, A.; Beugholt, C.; Kögerler, P.; Bögge, H.; Bud'ko, S.; Luban, M. *Inorg. Chem.* **2000,** *39*, 5176–5177.
70. Lin, J.-M.; Mei, Z.-B.; Guo, C., et al. *J. Am. Chem. Soc.* **2024,** *146*, 22797–22806.
71. Nishimoto, Y.; Yokogawa, D.; Yoshikawa, H.; Awaga, K.; Irle, S. *J. Am. Chem. Soc* **2014,** *136*, 9042–9052.
72. Zhao, H.-Y.; Li, Y.-Z.; Zhao, J.-W.; Wang, L.; Yang, G.-Y. *Coord. Chem. Rev.* **2021,** *443*, 213966.
73. Li, Z.; Zhang, Z.; Hu, H.; Liu, Q.; Wang, X. *Nat. Synth.* **2023,** *2*, 989–997.
74. Bontchev, R. P.; Nyman, M. *Angew. Chem. Int. Ed.* **2006,** *45*, 6670–6672.
75. Huang, P.; Qin, C.; Su, Z.-M., et al. *J. Am. Chem. Soc.* **2012,** *134*, 14004–14010.
76. Yu, H.; Lin, Y.-D.; Huang, S.-L.; Li, X.-X., et al. *Angew. Chem. Int. Ed.* **2023,** *62*, e202302111.
77. Zhu, Z.-K.; Zhang, J.; Cong, Y.-C., et al. *Angew. Chem. Int. Ed.* **2022,** *61*, e202113381.
78. Lai, R.-D.; Zhang, J.; Li, X.-X.; Zheng, S.-T.; Yang, G.-Y. *J. Am. Chem. Soc.* **2022,** *144*, 19603–19610.
79. Tsunashima, R.; Long, D.-L.; Miras, H. N.; Gabb, D.; Pradeep, C. P.; Cronin, L. *Angew. Chem. Int. Ed.* **2010,** *49*, 113–116.
80. Jin, L.; Zhu, Z.-K.; Wu, Y.-L.; Qi, Y.-J.; Li, X.-X.; Zheng, S.-T. *Angew. Chem. Int. Ed.* **2017,** *56*, 16288–16292.
81. Hong, L.-H.; Yue, S.-N.; Huang, X., et al. *Angew. Chem. Int. Ed.* **2024,** *63*, e202404314.
82. Wu, Y.-L.; Li, X.-X.; Qi, Y.-J.; Yu, H.; Jin, L.; Zheng, S.-T. *Angew. Chem. Int. Ed.* **2018,** *57*, 8572–8576.
83. Guo, Z.-W.; Lin, L.-H.; Ye, J.-P., et al. *Angew. Chem. Int. Ed.* **2023,** *62*, e202305260.
84. Martin-Sabi, M.; Soriano-Lopez, J.; Winter, R. S., et al. *Nat. Catal.* **2018,** *1*, 208–213.
85. Wu, Y.-L.; Du, J.; Zhang, H.-Y., et al. *Nano Res.* **2024,** *17*, 8261–8268.
86. Zheng, Q.; Kupper, M.; Xuan, W., et al. *J. Am. Chem. Soc.* **2019,** *141*, 13479–13486.
87. Xu, M.; Wang, T.; Zhang, W., et al. *Inorg. Chem. Front.* **2024,** *11*, 6981–6987.
88. Zhang, D.; Wang, C.; Lin, Z., et al. *Angew. Chem. Int. Ed.* **2024,** *63*, e202320036.
89. Wu, S.; Fu, Y.; Gan, H., et al. *Inorg. Chem. Front.* **2025,** *12*, 1021–1027.
90. Wang, X.; Brunson, K.; Xie, H., et al. *J. Am. Chem. Soc.* **2021,** *143*, 21056–21065.
91. Yang, P.; Kortz, U. *Acc. Chem. Res.* **2018,** *51*, 1599–1608.
92. Chubarova, E. V.; Dickman, M. H.; Keita, B., et al. *Angew. Chem. Int. Ed.* **2008,** *47*, 9542–9546.
93. Christie, L. G.; Asche, S.; Mathieson, J. S.; Vila-Nadal, L.; Cronin, L. *J. Am. Chem. Soc.* **2018,** *140*, 9379–9382.
94. Xu, F.; Scullion, R. A.; Yan, J., et al. *J. Am. Chem. Soc.* **2011,** *133*, 4684–4686.
95. Ma, T.; Ma, X.; Lin, Z., et al. *Inorg. Chem.* **2023,** *62*, 13195–13204.
96. Bhattacharya, S.; Ma, X.; Mougharbel, A. S., et al. *Inorg. Chem.* **2021,** *60*, 17339–17347.

97. Bhattacharya, S.; Barba-Bon, A.; Zewdie, T. A., et al. *Angew. Chem. Int. Ed.* **2022,** *61*, e202203114.
98. Ling, J.; Wallace, C. M.; Szymanowski, J. E. S.; Burns, P. C. *Angew. Chem. Int. Ed.* **2010,** *49*, 7271–7273.
99. Burns, P. C.; Nyman, M. *Dalton Trans.* **2018,** *47*, 5916–5927.
100. Colliard, I.; Morrison, G.; zur Loye, H.-C.; Nyman, M. *J. Am. Chem. Soc.* **2020,** *142*, 9039–9047.
101. Oien-Odegaard, S.; Bazioti, C.; Redekop, E. A.; Prytz, O.; Lillerud, K. P.; Olsbye, U. *Angew. Chem. Int. Ed.* **2020,** *59*, 21397–21402.
102. Colliard, I.; Nyman, M. *Angew. Chem. Int. Ed.* **2021,** *60*, 7308–7315.
103. Colliard, I.; Brown, J. C.; Fast, D. B.; Sockwell, A. K.; Hixon, A. E.; Nyman, M. *J. Am. Chem. Soc.* **2021,** *143*, 9612–9621.
104. Feng, Y.; Zhao, M.; Yang, J., et al. *Angew. Chem. Int. Ed.* **2025,** *64*, e202505511.
105. Xu, Z.; Chen, K.; Li, M.; Hu, C.; Yin, P. *Chem. Commun.* **2020,** *56*, 5287–5290.
106. Li, M.-T.; Yang, X.-Y.; Li, J.-S., et al. *Inorg. Chem.* **2018,** *57*, 3865–3872.
107. Yonesato, K.; Ito, H.; Yokogawa, D.; Yamaguchi, K.; Suzuki, K. *Angew. Chem. Int. Ed.* **2020,** *59*, 16361–16365.
108. Chi, M.; Wei, J.; Zhao, Z., et al. *Angew. Chem. Int. Ed.* **2025,** *64*, e202424499.
109. Feng, Y.; Fu, F.; Zeng, L., et al. *Angew. Chem. Int. Ed.* **2024,** *63*, e202317341.
110. Zhao, Z.; Wei, J.; Lang, Z.-L., et al. *J. Am. Chem. Soc.* **2025,** *147*, 25107–25114.
111. Yonesato, K.; Yanai, D.; Yamazoe, S., et al. *Nat. Chem.* **2023,** *15*, 940–947.
112. Yonesato, K.; Yanai, D.; Yamaguchi, K., et al. *Chem. Eur. J.* **2025,** *31*, e202500877.
113. Kamachi, M.; Yonesato, K.; Okazaki, T., et al. *Angew. Chem. Int. Ed.* **2024,** *63*, e202408358.
114. Koizumi, Y.; Yonesato, K.; Kikkawa, S.; Yamazoe, S.; Yamaguchi, K.; Suzuki, K. *J. Am. Chem. Soc.* **2024,** *146*, 14610–14619.
115. Wang, Z.; Sun, H.-T.; Kurmoo, M., et al. *Chem. Sci.* **2019,** *10*, 4862–4867.
116. Zhang, S.-S.; Chen, J.-Y.; Li, K., et al. *Chem. Mater* **2021,** *33*, 9708–9714.
117. Wang, Z.; Zhu, Y.-J.; Li, Y.-Z., et al. *Nat. Commun.* **2022,** *13*, 1802.
118. Rui, G.; Cai, P.-W.; Cai, S.; Sun, Y.-Q.; Li, X.-X.; Zheng, S.-T. *Chem. Sci.* **2024,** *15*, 12543–12549.
119. Guo, J.; Liu, J.; Cui, Y., et al. *Chem. Sci.* **2022,** *13*, 5718–5725.
120. Li, X.-X.; Zhao, D.; Zheng, S.-T. *Coord. Chem. Rev.* **2019,** *397*, 220–240.
121. Guo, J.; Chang, Q.; Liu, Z., et al. *Chem. Sci.* **2021,** *12*, 7361–7368.
122. Gan, H.; Bao, L.; Xu, N., et al. *Adv. Sci.* **2025,** *12*, 2408863.
123. Tong, K.-W.; Wang, Y.-H.; Du, J., et al. *Angew. Chem. Int. Ed.* **2025,** *64*, e202504424.
124. Zhu, M.; Han, S.; Liu, J., et al. *Angew. Chem. Int. Ed.* **2022,** *61*, e202213910.
125. Li, C.; Yamaguchi, K.; Suzuki, K. *Angew. Chem. Int. Ed.* **2021,** *60*, 6960–6964.
126. Li, C.; Mizuno, N.; Yamaguchi, K.; Suzuki, K. *J. Am. Chem. Soc.* **2019,** *141*, 7687–7692.
127. Yamaguchi, M.; Shioya, K.; Li, C., et al. *J. Am. Chem. Soc.* **2024,** *146*, 4549–4556.
128. Zhang, Z.; Liu, Y.-W.; Tian, H.-R., et al. *Matter* **2020,** *2*, 250–260.
129. Huang, X.; Zhou, Z.; Qin, L., et al. *Inorg. Chem.* **2023,** *62*, 5565–5575.
130. Zhao, Q.; Zeng, Y.; Jiang, Z., et al. *Angew. Chem. Int. Ed.* **2024,** *63*, e202421132.
131. Huang, Q.; Niu, Q.; Li, X.-F., et al. *Sci. Adv.* **2022,** *8*, eadd5598.
132. Yang, P.; Zhao, W.; Shkurenko, A., et al. *J. Am. Chem. Soc.* **2019,** *141*, 1847–1851.
133. Hou, T.; Xu, W.; Pei, X.; Jiang, L.; Yaghi, O. M.; Persson, K. A. *J. Am. Chem. Soc.* **2022,** *144*, 13446–13450.
134. Wang, X.; Li, S.; Wu, F., et al. *Angew. Chem. Int. Ed.* **2025,** *64*, e202416735.
135. Wang, M.-M.; Cai, J.-J.; Lun, H.-J., et al. *Adv. Funct. Mater* **2024,** *34*, 2311912.
136. Wang, N.-H.; Zhang, B.-Y.; Wu, X.-S., et al. *Chem. Eng. J.* **2024,** *498*, 155821.

137. Lu, M.; Zhang, M.; Liu, J., et al. *J. Am. Chem. Soc.* **2022,** *144*, 1861–1871.
138. Zhang, H.; Liu, W.; Li, A., et al. *Angew. Chem. Int. Ed.* **2019,** *58*, 16110–16114.
139. Lan, G.; Ni, K.; Veroneau, S. S.; Luo, T.; You, E.; Lin, W. *J. Am. Chem. Soc.* **2019,** *141*, 6859–6863.
140. Wang, L.; Dai, P.; Ma, H.; Sun, T.; Peng, J. *Inorg. Chem. Front.* **2024,** *11*, 1339–1365.
141. Falaise, C.; Khlifi, S.; Bauduin, P., et al. *Angew. Chem. Int. Ed.* **2021,** *60*, 14146–14153.
142. Liu, C.-L.; Moussawi, M. A.; Kalandia, G., et al. *Chem. Int. Ed.* **2024,** *63*, e202401940.
143. Chen, W.-J.; Liu, C.-Y.; Mu, Y.-J., et al. *Am. Chem. Soc.* **2025.** https://doi.org/10.1021/jacs.1025c06495.
144. Chen, J.; Bera, M. K.; Li, H., et al. *Angew. Chem. Int. Ed.* **2021,** *60*, 5833–5837.
145. Cameron, J. M.; Guillemot, G.; Galambos, T., et al. *Chem. Soc. Rev.* **2022,** *51*, 293–328.
146. Luo, J.; Zhang, B.; Yvon, C., et al. *Eur. J. Inorg. Chem.* **2019**, 380–386.
147. Liu, Z.; Qian, K.; Liu, T.; Tsige, M. *Chem. Commun.* **2022,** *58*, 12151–12159.
148. Falaise, C.; Khlifi, S.; Bauduin, P., et al. *J. Am. Chem. Soc.* **2024,** *146*, 1501–1511.
149. Wan, C.; Wu, Y.; Cheng, Q., et al. *J. Am. Chem. Soc.* **2023,** *145*, 25431–25439.
150. Zhang, S.; Shi, W.; Wang, X. *Science* **2022,** *377*, 100–104.
151. Liu, Q.; Wang, X. *Matter* **2020,** *2*, 816–841.
152. Nie, S.; Wu, L.; Wang, X. *J. Am. Chem. Soc.* **2023,** *145*, 23681–23690.
153. Liu, Q.; Sheng, Z.; Shi, W.; Cheng, X.; Xu, X.; Wang, X. *J. Am. Chem. Soc.* **2024,** *146*, 12819–12827.
154. Liu, Q.; Wang, X. *Angew. Chem. Int. Ed.* **2023,** *62*, 202217764.
155. Liu, J.; Li, Y.; Chen, Z., et al. *J. Am. Chem. Soc.* **2022,** *144*, 23191–23197.
156. Ge, H.; Zheng, L.; Yuan, G., et al. *J. Am. Chem. Soc.* **2024,** *146*, 10735–10744.
157. Marcano, D. E. S.; Parac-Vogt, T. N. *Coord. Chem. Rev.* **2024,** *518*, 216086.
158. Lamare, R.; Ruppert, R.; Boudon, C.; Ruhlmann, L.; Weiss, J. *Chem. Eur. J.* **2021,** *27*, 16071–16081.
159. Ma, M.; Chen, J.; Dong, L., et al. *J. Inorg. Biochem.* **2025,** *262*, 112739.
160. Zhao, Y.; Liu, Z.; Qin, Z., et al. *Angew. Chem. Int. Ed.* **2025,** *64*, e202505564.
161. Abdelhameed, S. A. M.; de Azambuja, F.; Vasovic, T.; Savic, N. D.; Cirkovic Velickovic, T.; Parac-Vogt, T. N. *Nat. Commun.* **2023,** *14*, 486.
162. She, S.; Bell, N. L.; Zheng, D., et al. *Chem* **2022,** *8*, 2734–2748.
163. Kondinski, A.; Gumerova, N. I.; Rompel, A., et al. *Chem. Eur. J.* **2025,** *31*, e01528.
164. He, D.; Jiang, Y.; Guillen-Soler, M., et al. *J. Am. Chem. Soc.* **2024,** *146*, 28952–28960.
165. Guo, H.; He, D.; Long, D.-L.; Cronin, L. *Chem. Commun* **2025,** *61*, 7121–7124.
166. Huang, L.; Zhang, C.; Fu, Y., et al. *J. Am. Chem. Soc.* **2025,** *147*, 23014–23025.
167. Yin, J.-F.; Amidani, L.; Chen, J., et al. *Angew. Chem. Int. Ed.* **2024,** *63*, e202310953.
168. Zhu, Z.; Wei, M.; Li, B.; Wu, L. *Dalton Trans.* **2021,** *50*, 5080–5098.